Article

Current Biology

Selective adhesion preserves eye patterning as axonal retinotopy in the *Drosophila* brain

Graphical abstract

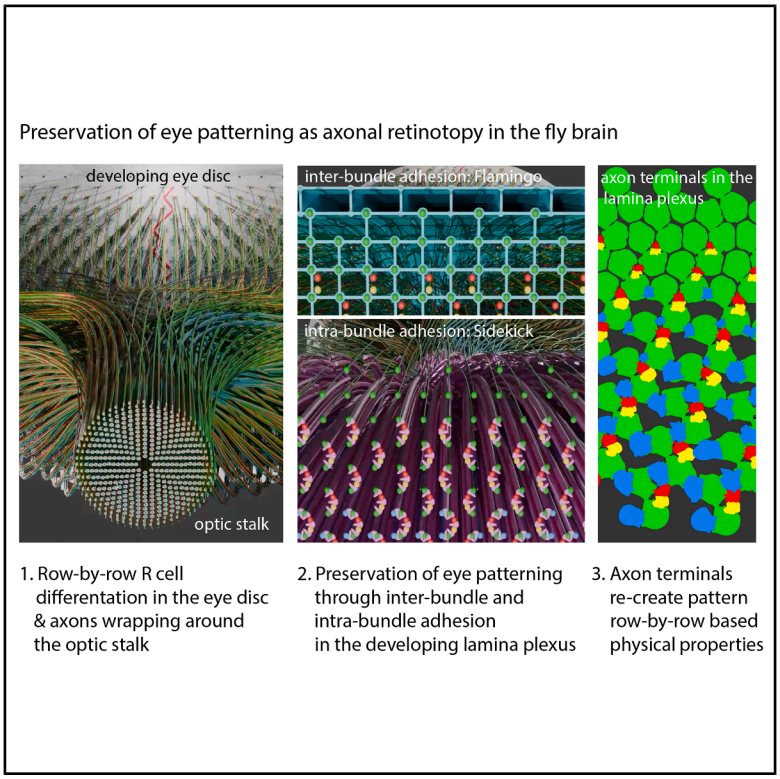

Highlights

- *Drosophila* retinotopy is based on precise preservation of eye patterning
- The temporal gradient of cell differentiation is preserved in axon outgrowth
- Inter- (Flamingo) and intra-bundle (Sidekick) adhesion maintain axon adjacencies
- Computational models show how flexible adhesive axon terminals produce the pattern

Authors

Melinda Kehribar, Charlotte B. Wit, Ksenia Krasikova, ..., Lasse Q. Wriedt, Max von Kleist, P. Robin Hiesinger

Correspondence

robin.hiesinger@fu-berlin.de

In brief

Kehribar et al. present a mechanism based on axon-axon interactions for the target-independent development of retinotopic axonal projections in the *Drosophila* brain. A temporal gradient as well as two adhesive forces ensure retinotopic mapping. Computational models reveal the role of flexible adhesive surfaces for pattern generation in the brain.

Kehribar et al., 2026, Current Biology *36*, 1–18
March 9, 2026
https://doi.org/10.1016/j.cub.2026.01.007

CellPress

Please cite this article in press as: Kehribar et al., Selective adhesion preserves eye patterning as axonal retinotopy in the *Drosophila* brain, Current Biology (2026), https://doi.org/10.1016/j.cub.2026.01.007

Current Biology

CellPress
OPEN ACCESS

Article

Selective adhesion preserves eye patterning as axonal retinotopy in the *Drosophila* brain

Melinda Kehribar,[1] Charlotte B. Wit,[1] Ksenia Krasikova,[1] Egemen Agi,[1] Eric T. Reifenstein,[2] Neele Wolterhoff,[1] Lasse Q. Wriedt,[1,3] Max von Kleist,[2] and P. Robin Hiesinger[1,4,*]
[1]Division of Neurobiology, Free University of Berlin, 14195 Berlin, Germany
[2]Department of Mathematics, Free University of Berlin, 14195 Berlin, Germany
[3]Faculty of Engineering, Computer Science and Psychology, Ulm University, 89081 Ulm, Germany
[4]Lead contact
*Correspondence: robin.hiesinger@fu-berlin.de
https://doi.org/10.1016/j.cub.2026.01.007

SUMMARY

Flies, like vertebrates, preserve the spatial organization of visual input through axonal projections into the brain, a principle called retinotopy. The best-known developmental mechanisms for retinotopy are molecular gradients in the target regions, yet *Drosophila* photoreceptors can form retinotopic maps ectopically in wrong brain regions. We show that a temporal gradient of axonal growth plus selective adhesion between photoreceptor axons precisely preserves the cellular eye pattern. Each of the 800 single eyes, the ommatidia, form a bundle of six axons that are held in place by inter-bundle adhesion through the protocadherin Flamingo and preserve their intra-bundle organization through the adhesion molecule Sidekick. Computational modeling of axon terminals as selectively adhesive soft bodies in a developmental wave generates the retinotopic pattern, including the shapes of the postsynaptic lamina neurons, which emerge without explicit encoding. Hence, a temporal gradient and two adhesive forces can ensure retinotopic map formation without a target-derived mechanism.

INTRODUCTION

Retinotopy describes the precise mapping of neighboring visual inputs in the eye as neighboring connectivity pattern in the brain.[1] The study of retinotopic projections has been a cornerstone of developmental and sensory neuroscience for decades. Axon-target interactions, in particular target-derived molecular gradients, are the best understood mechanism for the development of axonal retinotopy.[2–6] By contrast, we have recently shown that *Drosophila* photoreceptor axons can form retinotopic maps in ectopic brain regions.[7] This observation suggests that the arrangement of axons between the eye and the brain is precisely preserved, but the underlying molecular and cellular mechanisms have remained unclear.

Axon-axon interactions contribute to retinotopic map formation in all systems analyzed to date. In vertebrate visual systems, axon-axon interactions were characterized in the 1980s and later found to function together with molecular gradients in the relative positioning of axons in the brain.[8–10] Similar target-independent roles for axonal pre-patterning have been described in visual and olfactory systems in both vertebrates and flies.[11–14]

In *Drosophila*, the retinotopic map is a transient state prior to re-sorting into a so-called visuotopic map according to the principle of neural superposition[15,16] (Figures 1A–1C). Strict retinotopy in *Drosophila*, as in all *Brachycera*, can therefore only be observed in the developmentally transient lamina plexus, a sheet of growth cones where retinotopically organized axons are subsequently re-sorted to establish visuotopy (Figure 1C).[7,17]

The temporal order of axonal growth plays an important role in mapping projections from the eye to the brain in all systems studied to date.[8,10,12,18,19] In *Drosophila*, a wave of cellular differentiation leads to row-by-row patterning of the eye disc, an epithelium of undifferentiated cells. Through this mechanism, a row of ~10–20 simultaneously developing single eyes, the ommatidia, is added every ~2 h.[20–22] In each ommatidium, eight photoreceptor neurons (R cells) differentiate in a temporal order that translates into a stereotypic arrangement.[23–25] Six of these R cells (R1–6) from each ommatidium form the retinotopic map in the lamina plexus. To what extent axonal growth follows the row-by-row R1–6 differentiation and patterning of the eye disc has remained unclear.

Here, we show that the pattern of R1–6 differentiation in the eye is preserved as axonal retinotopy in the brain. Instead of molecular gradients, the temporal gradient of row-by-row differentiation and axonal growth provides an organizing principle in time. Mechanistically, two distinct and complementary adhesive forces are required for this process, inter-bundle and intra-bundle. We identified the homophilic cell adhesion molecules Flamingo and Sidekick as these adhesive forces, respectively.

RESULTS

The probabilistic, unique equator of an individual eye is preserved in the axonal projections in the brain

The *Drosophila* eye is an almost perfectly patterned structure, except for the probabilistically zigzagging line that separates the dorsal and ventral halves of the eye mirror-symmetrically

Please cite this article in press as: Kehribar et al., Selective adhesion preserves eye patterning as axonal retinotopy in the *Drosophila* brain, Current Biology (2026), https://doi.org/10.1016/j.cub.2026.01.007

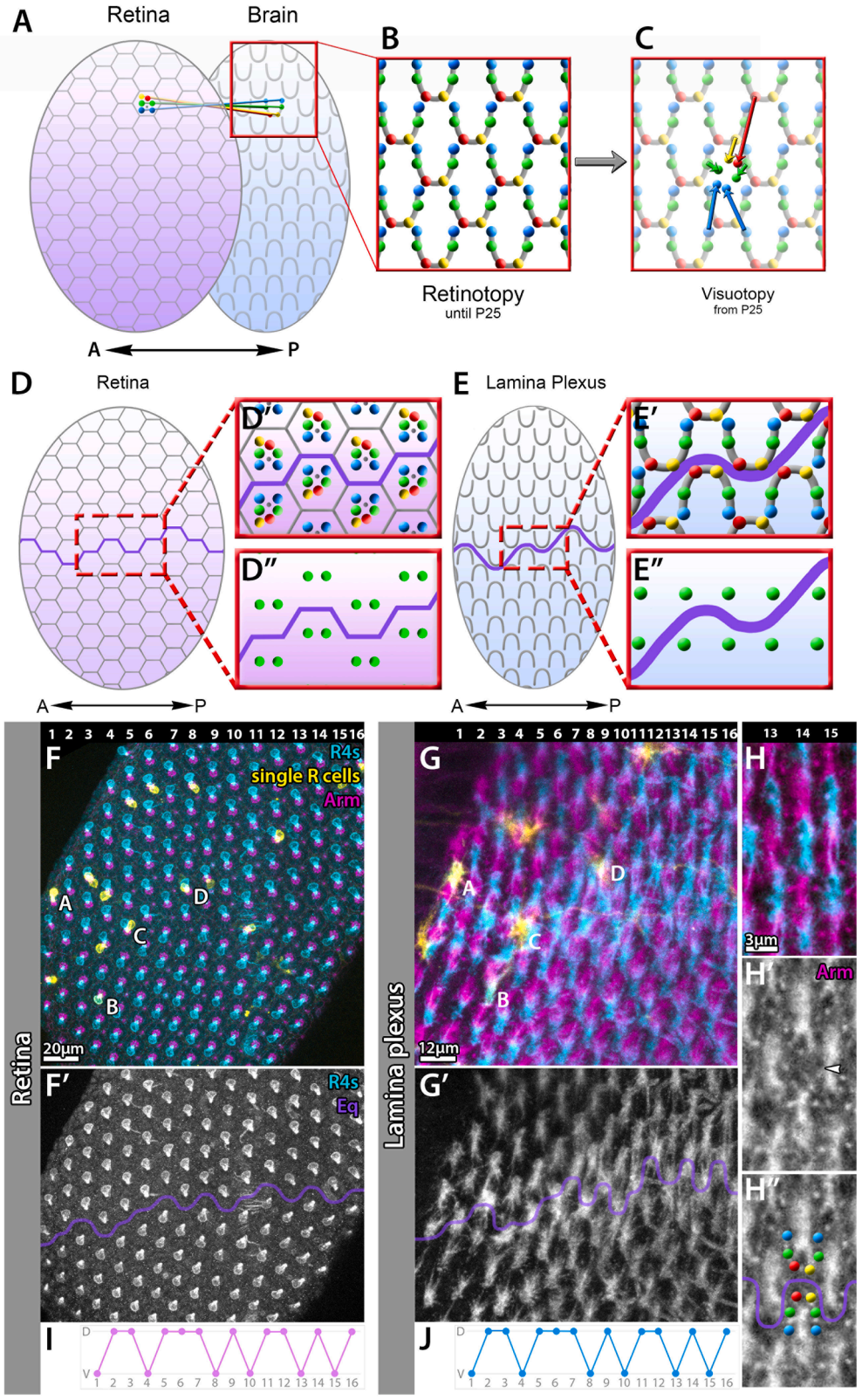

(legend on next page)

Please cite this article in press as: Kehribar et al., Selective adhesion preserves eye patterning as axonal retinotopy in the *Drosophila* brain, Current Biology (2026), https://doi.org/10.1016/j.cub.2026.01.007

(Figures 1D and 1E). An individual eye's uniquely zigzagging equator line is an opportunity to test a fundamental mechanistic question about the development of retinotopic mapping between the eye and the brain: to what extent does the cell pattern in the eye determine the axonal pattern in the brain? If the equator line of an individual eye has the identical zigzag pattern as that eye's axonal projections in the brain, then it must have been preserved from the cell bodies to the axon terminals. By contrast, if the axonal retinotopic map is guided by local molecular mechanisms in the target region, then the probabilistic zigzag line should not be preserved in the brain.

We identified the corresponding regions of cell bodies in an individual eye and the axonal projections in the lamina plexus at developmental stage P35 using the relative positions of sparsely labeled single growth cones. As shown in the example in Figures 1F and 1G, the pattern of sparsely labeled cell bodies marked A–D (Figure 1F) matches the corresponding growth cones (A–D in Figure 1G). Next, we used labeling of all R4 cell bodies (Figure 1F′) and growth cones (Figure 1G′) to identify the equator. We additionally used Armadillo (Arm) staining (Figures 1H and 1H′) to validate the equator based on the mirror-symmetric arrangement of R1–6 axon terminal bundles. In the example shown in Figures 1F and 1G we mapped the equator across 16 rows in the eye and the matching 16 rows in the lamina plexus. We found the zigzag pattern in the eye to be fully preserved in the brain in this and three other cases (Figures 1I, 1J, and S1A–S1N). The "zigzagging" switches neither occur with 100% probability, nor randomly (50%); we therefore calculated the probability p to switch between the dorsal vs. ventral direction ($1 \rightarrow 0$ or $0 \rightarrow 1$) and $1 - p$, the probability of the equator line to continue in the same direction ($1 \rightarrow 1$ or $0 \rightarrow 0$). Across samples (Figures 1F, 1G, and S1A–S1J), we calculated $p = 0.87$ [0.81, 0.91] (Wilson confidence interval), i.e., a likelihood that is higher, but less than 100%, to switch than to stay in the same direction. For the sequence from Figures 1F and 1G, the probability of a random match between the eye and brain (with $p = 0.87$) is $0.5 \times p\hat{}11 \times (1 - p)\hat{}4 \approx 0.00003$. For the samples shown in Figure S1, the corresponding probabilities are 0.012, 0.008, and 0.001. We conclude that molecular and cellular mechanisms must exist that ensure the exact preservation of the retinal pattern in the brain.

R2/5 axons generate an equator-blind orthogonal pattern marked by the cell adhesion molecule Flamingo in the lamina plexus

The development of the ommatidial pattern has been studied in great detail, including the mirror-symmetric arrangement along the equator through planar cell polarity (PCP) (Figure 2A).[26,27] The row-by-row differentiation of R cells, beginning with R8, then R2/5, R3/4, and lastly R1/6 (Figure 2B) may translate into a corresponding series of rows of axons growing toward the brain, as suggested previously for larger flies.[21] Among these pairs, only R3 and R4 are known to differ both molecularly and in their asymmetric arrangement in the ommatidia, while R2/5 and R1/6 may be pairs of identical or very similar cells.[28–30] The differentiation of R3/R4 first defines the equator, which separates mirror-symmetric dorsal and ventral halves of the eye with a probabilistic zigzag line (Figures 2A and 2B). In the final arrangement, the pattern of R2s and R5s does not reveal the equator (Figures 1D'' and 1E''), while R3/4 on one side and R1/6 on the other are mirror-symmetrically arranged in both the eye and the axonal projections (Figures 1D′ and 1E′).

The equator only forms after R3/4 differentiate and ommatidia at the 5-cell stage (R8 + R2/5 + R3/4) rotate either clockwise or counterclockwise on either side of the equator (Figure 2A). Since axon terminals preserve the eye equator that is generated by the rotation of developing ommatidia, the start of ommatidial rotations must precede axon outgrowth. Rotation of the ommatidial bundles occurs in two steps of ~45 degree rotations, opening a time window for axon outgrowth of R2/5 followed by (or together with) R3/4, of around 4–5 h.[31] During their outgrowth toward the brain, the axon bundles further rotate 180°; as a result, R3/4 cell bodies that point away from the equator (Figures 1D′ and 1F′) correspond to growth cones that point toward the equator in the lamina plexus (Figures 1E′ and 1G′).[32]

The anterior-to-posterior axis reveals the temporal progression of R axon terminals in the lamina plexus at pupal stage P15 (Figures 2C and S1O). In the first recognizable, anterior-most row we could not distinguish the number or pattern of R cell axons per bundle (Figure 2C, row +1); however, L cell neurites (green) are already present in a zigzag line (Figure 2C, arrow). R axon terminals were identified based on absence of the R cell membrane marker and Arm labeling as previously described[7] (STAR Methods). The next posterior row (+2) already exhibits four clearly recognizable axons per bundle, indicative of R2/5 + R3/4. In the next three rows (+3 to +5), bundles contain four discernible axon terminals, as previously seen in electron micrographs.[33] These 4R bundles are diagonally and mirror-symmetrically arranged, thus marking the equator directly after arrival in the brain (Figures 2C, 2C′, and S1O). Starting in row +6, two more axons are added in the stereotypic positions of R1/R6 to complete the retinotopic pattern (Figures 2C and 2C′′). These observations are consistent with electron microscopy of the lamina plexus indicating several rows of bundles with four axons in younger regions and six axon terminals in older regions.[33] Our data suggest that R1–6 axons arrive in the brain in a temporal succession of rows that follows the R cell differentiation in the developing eye and preserves the equator.

By P25 the temporal wave of retinotopic axonal patterning in the lamina plexus has concluded and the equator is clearly

Figure 1. The probabilistic, unique equator of an individual eye is preserved in the axonal projections in the brain

(A–C) Bundles of six R cell axons retinotopically map to the brain (A). Starting at P25, retinotopy (B) is corrected to visuotopy (neural superposition) (C).

(D and E) Dorsal and ventral halves of the retina (D) and lamina plexus (E) are mirror-symmetrically arranged on both sides of the equator (purple). Insets show that R2/5 cells are equidistant to each other, even across the equator, in both (D′′) and (E′′).

(F–H) Retina (F) and corresponding lamina plexus (G) of the same optic lobe reveal equator pattern is preserved. Corresponding regions were identified using R4 labeling (cyan; F′ and G′) and Arm staining (magenta; H–H′′).

(I and J) Equator plots of the retina (I) and corresponding lamina plexus (J) are identical. Stage P35, $n = 4$.

See also Figure S1 and Table S1.

Please cite this article in press as: Kehribar et al., Selective adhesion preserves eye patterning as axonal retinotopy in the *Drosophila* brain, Current Biology (2026), https://doi.org/10.1016/j.cub.2026.01.007

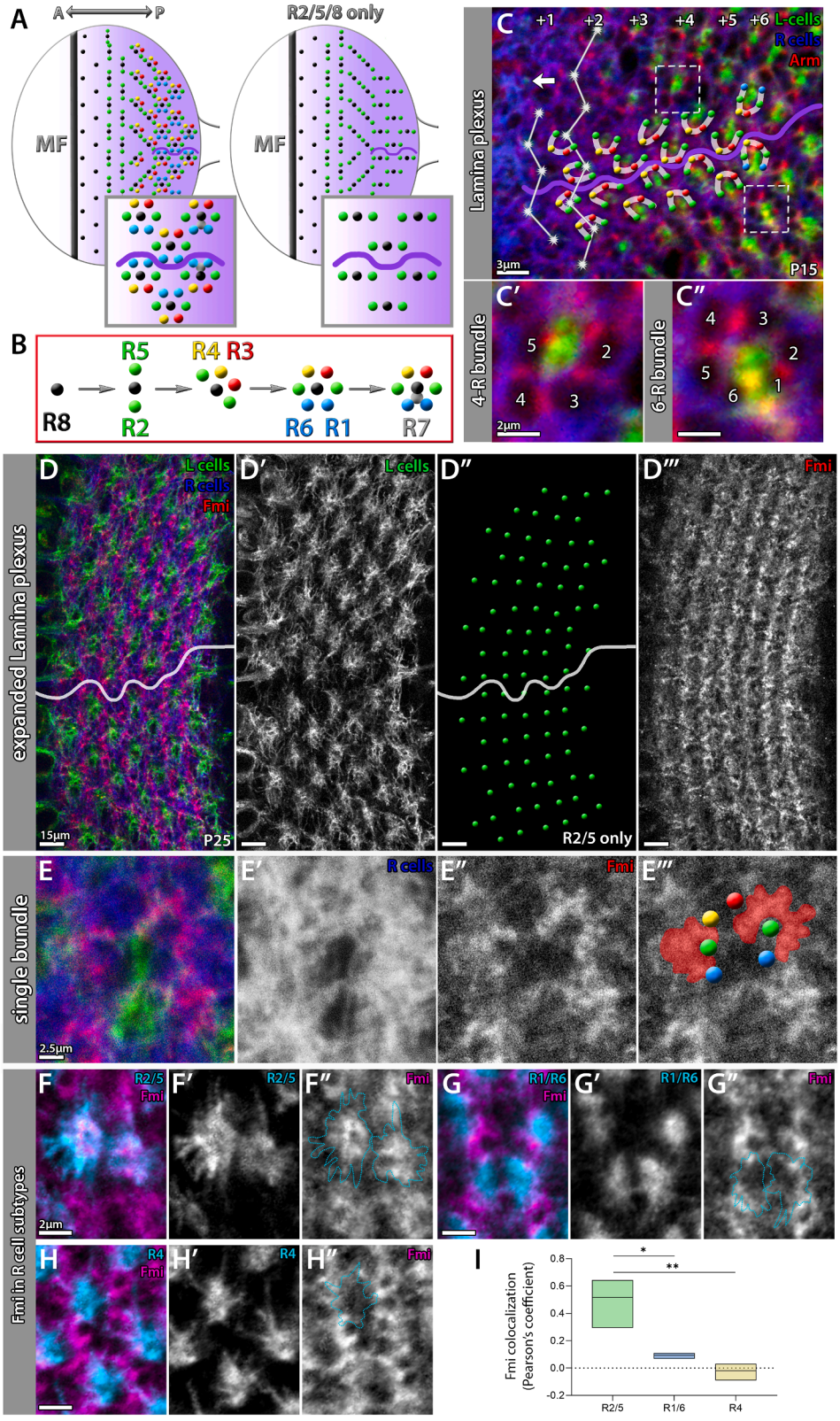

(legend on next page)

Please cite this article in press as: Kehribar et al., Selective adhesion preserves eye patterning as axonal retinotopy in the *Drosophila* brain, Current Biology (2026), https://doi.org/10.1016/j.cub.2026.01.007

visible in the pattern of the L cells, R3/4 and R1/6 (Figures 2D and 2D′; compare with Figure 1E). Remarkably, R2/5 retain an equator-blind pattern in the eye disc, eye, and lamina plexus (Figures 2A and 2D′′). In contrast to the hexagonal arrangement of ommatidia and R1–6 bundles in the brain, the R2/5 pattern resembles an orthogonal, "equator-blind" grid (Figure 2D′′). We reasoned that an inter-bundle R2/5-specific adhesive force should exist that allows R2/5 axons to establish and maintain this grid across bundles, since R2/5s are the first-arriving axons in the lamina plexus.

We screened a panel of antibodies against cell adhesion molecules known to function in visual map formation and used expansion microscopy and co-labeling of R1–R6 and L cells. We found that the protocadherin Flamingo (Fmi) labels a unique, equator-blind orthogonal pattern at P25 (Figures 2D–2D′′′). Fmi is expressed in a ring-like shape around the presumptive R2/5 axon terminal "heel" positions (Figures 2E–2E′′′). Co-labeling of specific R subtypes using drivers that sparsely label R2/5 (Figure 2F), all R1/6 (Figure 2G), or R4 (Figure 2H) together with anti-Fmi immunolabeling revealed strong colocalization with R2/5, weak colocalization with R1/6, and none with R4, similar to previous findings.[34] (Figure 2I; additional representative examples in Figures S1P–S1X.) The absence of Fmi in R3/R4 axon terminals is remarkable because Fmi functions specifically in R3/4 cell bodies (but not R2/5 or R1/6) in the eye disc to establish PCP.[35–38] In axons, an early role of Fmi is supported by its localization to the first row of axons arriving in the brain, which was previously interpreted as specific to R8.[39,40] Based on these and our observations, we hypothesized that Fmi has a distinct function in the growth cones of the first-arriving R8/2/5 and subsequently R1/6, and that this function is independent from Fmi's role in R3/4 cell bodies during earlier eye development.

Fmi is required in early arriving R2/5 axons to create and maintain an inter-bundle scaffold in the lamina plexus

Previous analyses indicated that retinotopic organization is preserved in the optic stalk, with younger axons on the outside and older axons in the center.[41,42] We generated an mCherry-pHluorin knockin in the endogenous *fmi* locus to label all Fmi protein that could engage in adhesive interactions (Figure S2A). The Fmi protein has high turnover rates,[43] and the mCherry-pHluorin tag distinguishes Fmi in degradative compartments (mCherry only) from potentially active Fmi (pHluorin), including on the cell surface[44] (Figures S2B and S2C). The knockin is viable and has no obvious defects (Figure S2D), indicating that the tagged Fmi is functional. We found that Fmi-pHluorin labels the circumference but not the center of the optic stalk (Figures 3A and 3B′). After entering the larval brain, the axons of the optic stalk defasciculate and spread out into a single row of Fmi-positive axons in the outermost, i.e., youngest, row (Figure 3C). Correspondingly, Fmi is expressed at high levels only in the first row of R cell axons (Figures 3D and 3E′′; arrowhead in Figure 3E). These findings suggest that new rows of differentiating R cells are wrapped around the optic stalk, creating an onion-like layering in which only the newest, outermost row is Fmi positive.

While Fmi is downregulated from axons after the first row, the Fmi-pHluorin signal remains active in axon terminals across the lamina plexus (Figures S2E–S2G; compare also the R2/5 pattern shown with Fmi antibody labeling in Figure 2D′′′). Live imaging of the developing lamina plexus reveals high levels of Fmi until P35, just before the lamina plexus is known to disintegrate[7] (Figures S2F–S2H; Video S1). These findings suggest that Fmi adhesion between the R2/5s of adjacent bundles maintains the retinotopic map in axons during neural superposition development in the lamina plexus.

Fmi in the youngest axons arriving in the lamina plexus can be abolished by knocking down *fmi* using a sparse R8/2/5-specific driver line (Figures 3F and S2I), consistent with a previous characterization of Fmi in R8s in the first row.[39,40] To test whether R2/5 axons may contribute to the first row of Fmi-positive axons innervating the lamina plexus we used R8-specific RNAi (R8-specific *sensFlp* with *GMR-FRT-stop-FRT-Gal4*). This reduced Fmi levels in R8 axon terminals to background levels (Figure S2J) yet signal in the youngest row of lamina plexus axons remained (Figure S2K). Similarly, knockdown with R1/6 or R3/4 driver lines did not result in a loss of Fmi on the earliest axons (Figures S2L–S2N). These data suggest that R2/5 axons, in addition to R8, may be Fmi positive in the youngest row supplying the lamina plexus.

fmi knockdown using a sparse R2/5 driver led to a correspondingly sparse downregulation in the lamina plexus at P25 (Figures 3G, S2O, and S2P). Additional knockdown in R1/6s further reduced Fmi levels, with the remaining Fmi in the characteristic ring-like pattern around R2/5s not affected due to the sparse R2/5 knockdown (arrowhead in Figures 3H, S2Q, and S2R). Correspondingly, RNAi only with the R1/6-specific driver reduced overall Fmi levels in the lamina plexus but left R2/5 rings intact (Figures S2S and S2T), whereas R3/4-specific RNAi did not affect the Fmi pattern (Figures S2U and S2V). We conclude that Fmi localizes to R8/2/5 axons until they reach the lamina plexus before being downregulated on the axons but remains present around R2/5 terminals across all rows of the lamina plexus.

Figure 2. R2/5 axons generate an equator-blind orthogonal pattern marked by the cell adhesion molecule Flamingo in the lamina plexus

(A and B) The eye disc develops in a temporal wave following the morphogenetic furrow (MF, black) from anterior to posterior. (A) The equator emerges after R3/4 cell differentiation and ommatidia rotate either clockwise or counterclockwise (left, inset). The R8/2/5 pattern remains equator-blind at all times (right, inset). (B) In each row, R cells develop in a sequence: R8 (black), R2/5 (green), R3/4 (red/yellow), R1/6 (blue), and R7 (gray).

(C) At P15, the lamina plexus exhibits a similar row-by-row temporal gradient. In younger rows, axonal bundles contain four R cells, likely R2/5 + R3/4 (magnified example from row +4 in C′), whereas older rows contain all six (magnified example from row +6 in C′′). $n = 6$.

(D and E) In the fully developed lamina plexus at P25, L cell (green; D′) and R cell (blue) patterns reveal the equator (white), whereas the R2/5 pattern resembles an orthogonal equator-blind grid (D′′). Fmi antibody staining (red; D′′′) marks a similar pattern. In a single bundle, Fmi is expressed in a ring-like shape around R2/5 heels (E–E′′′). $n = 27$.

(F and G) Subtype-specific labeling of R cells (cyan) reveals strong overlap of Fmi (magenta) with R2/5 (F), less with R1/6 (G), and no overlap with R4 (H). Stage P25; $n = 4$, 10, and 4, respectively.

(I) Quantification shows strong colocalization of Fmi labeling with R2/5. Lines in boxplots represent median. $^{*}p = 0.0104$, $^{**}p = 0.029$. $n = 3$ per subtype.

See also Figure S1 and Table S1.

Please cite this article in press as: Kehribar et al., Selective adhesion preserves eye patterning as axonal retinotopy in the *Drosophila* brain, Current Biology (2026), https://doi.org/10.1016/j.cub.2026.01.007

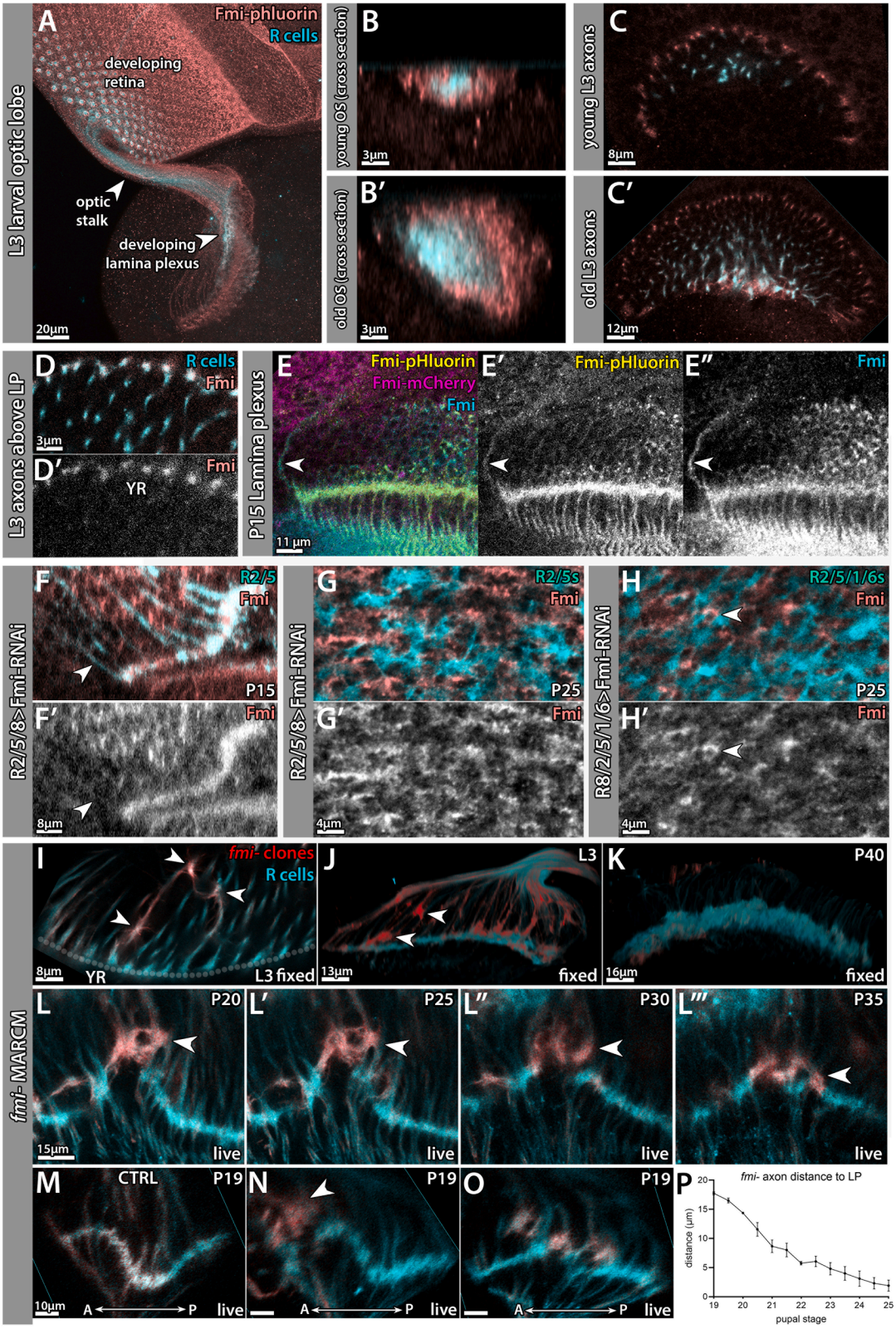

(legend on next page)

Please cite this article in press as: Kehribar et al., Selective adhesion preserves eye patterning as axonal retinotopy in the *Drosophila* brain, Current Biology (2026), https://doi.org/10.1016/j.cub.2026.01.007

To investigate the role of axonal Fmi, we analyzed single *fmi* mutant R cell axons prior to arrival in the lamina plexus. As shown in Figures 3I and 3J, *fmi* mutant axons appear stalled or delayed during larval stages, in the anterior-most, youngest row of axons. We were surprised by this axonal growth defect, because previous findings had shown that single *fmi* mutant R cell axons exhibited no defects at later time points and in the adult.[45] Indeed, when we tested single mutant R1–6 cells for each subtype during later development, we found no defects (Figures 3K, S3A, and S3B). To observe the developmental fate of delayed *fmi* mutant axons, we performed live imaging of *fmi* mutant clones of various sizes. We found delayed R cell axons for single *fmi* mutant axons and small clusters of mutant axons; such mutant growth cones initially stall without integration into the lamina plexus but are subsequently "pulled into" the growth cone layer (Figures 3L–3L‴ and 3P; Video S2). Delayed mutant axons were present in all regions of the lamina plexus, including the youngest, anterior-most side (Figures 3M–3O). These observations suggest that loss of *fmi* can lead to temporal delays and growth defects that are compensated for during subsequent development.

Fmi is required for inter-bundle, but not intra-bundle adhesion independent of known signaling functions

While single *fmi* mutant axons end up in the correct position (Figures S3A and S3B), large mutant clones (>5 bundles) led to holes in the lamina plexus (Figures 4A, 4B, and S4E). Similarly, R2/5/1/6 knockdown of *fmi* led to gaps between bundles (Figure S4A), and larger mutant clones led to larger gaps (Figures S4B–S4E). The variance in bundle distance steadily increased with growing clone size (Figure S4E). Mutant R1/6 axons (using GMRFlp) did not cause inter-bundle defects in the lamina plexus (Figures S4H and S4H″) or axon arrival defects (Figure S4I). We conclude that Fmi's inter-bundle role is required early and is specific to R8 and R2/5. By contrast, maintenance of the inter-bundle grid throughout later developmental stages might depend on R2/5 and R1/6, as both pairs express Fmi once they have arrived in the lamina plexus (Figures 2E–2H); Fmi signal is reduced in R1/6-specific knockout and knockdown experiments (arrowhead in Figures S4H′, S2S, and S2T). These observations suggest that adhesion between bundles is required to maintain the retinotopic pattern in the lamina plexus.

Fmi is known to be both a homophilic cell adhesion molecule[46] as well as an adhesion G protein-coupled receptor[47] in PCP signaling, where it functions in a complex with the receptor Frizzled (Fz).[35,36,48] Loss of *fmi* or *fz* in R cells leads to identical ommatidial rotation defects that are preserved as axon bundle rotations in the lamina plexus[49] (red arrows in Figures 4C″, S4F, and S4G′). However, loss of *fz* does not cause delayed axonal arrival or holes in the lamina plexus (Figure 4C). An alternative PCP signaling mechanism requires Dachsous (Ds)[50–55]; similar to *fz*, clones mutant for *ds* exhibited no defects (Figures 4C and 4D), except for irregularities of the Fmi pattern in regions with bundle rotations (compare red arrows in Figures 4C″, 4C‴, and S4J). Together, these data do not support a canonical PCP signaling function similar to R3/R4 cell bodies in the eye but instead suggest an adhesive role of Fmi across R2/5 axon terminals.[56–58]

Intra-bundle organization in large *fmi* mutant clones remained largely intact as indicated by the presence and position of a single R4 within a six-terminal bundle (Figures 4E, 4F, and S5D–S5F). Hence, a separate and Fmi-independent mechanism needs to ensure the correct placement of R3/4 and R1/6 when they integrate into the early R2/5 scaffold.

The R1–6 intra-bundle organization is preserved through the homophilic cell adhesion molecule Sidekick

We first investigated the preservation of intra-bundle organization by analyzing whether wild-type R1–6 axons within an ommatidial bundle exhibit no "braiding," i.e., no axons crossing within a bundle, as suggested for larger flies.[21] We analyzed stretches of axonal bundles above the lamina plexus and found that R1–6 axons within a bundle exhibited an exquisite preservation of adjacencies along several micrometers of densely aligned bundles (Figures 5A, S5A, S5B, and S5D). This preservation of adjacencies suggests an adhesive mechanism that maintains precise relative axon positions between the eye and the brain.

The attachment points between R1–6 growth cones upon arrival in the lamina plexus are marked by the homophilic cell adhesion molecule Sidekick (Sdk)[59] (Figures S6A and S6B). Flies lacking *sdk* are viable but exhibit patterning defects in the developing lamina plexus[59] (Figures S6C–S6J). Antibody labeling of larval eye-brain complexes revealed high Sdk levels along the entire optic stalk, suggesting a role on R axons prior to reaching the lamina plexus (Figures 5C and 5D; same specimen with Fmi labeling in Figure 3D). While Fmi was restricted to the youngest row, Sdk localized to all axons equally (compare Figures 3D and 5D).

Figure 3. Fmi is required in early arriving R2/5 axons to create an inter-bundle scaffold in the lamina plexus

(A–C) Fmi-pHluorin (red) is expressed along the optic stalk connecting the eye and brain at larval stage L3 (A). Cross sections of the optic stalk reveal Fmi-pHluorin expression on the youngest, outermost layer (B). In the larval brain, bundles defasciculate and Fmi-pHluorin only labels the anterior-most row of axons above the lamina plexus (C). $n = 7$.

(D) At P15, Fmi antibody (red) also marks the youngest row (YR) of axons (cyan). $n = 6$.

(E) Sideview of the lamina plexus, showing Fmi-pHluorin (yellow) and Fmi antibody (cyan) both mark the youngest row of axons. $n = 5$.

(F–H) Fmi knockdown using a R2/5/8-specific driver (cyan) abolishes Fmi expression (red) in the youngest row of axons (arrowhead) at P15 (F). In the P25 lamina plexus, knockdown with the sparse R2/5/8 driver disrupts the orthogonal Fmi pattern (G). Combining this driver with a R1/6-specific driver abolishes almost all Fmi staining (H), except for rings in regions not affected by the drivers (arrowhead in H).

(I–K) Single *fmi*− axons (red) appear stalled above the lamina plexus (cyan) at larval stage L3 (I and J). $n = 12$. At pupal stage P40, the lamina plexus appears as a uniform layer (K).

(L) Live imaging of stalled *fmi*− axons reveals they are integrated into the lamina plexus throughout development (arrowheads). $n = 10$.

(M–O) Anterior-posterior views of control (M) and two experimental brains (N and O). Stalled *fmi*− axons can be observed on the youngest (arrowhead in N) and older regions of the lamina plexus (O).

(P) Quantification of *fmi*− axons integrating into the lamina plexus over time. Error bars represent SEM. $n = 3$ mutant patches from two flies.

See also Figure S2, Table S1, Videos S1 and S2, and Data S1.

Please cite this article in press as: Kehribar et al., Selective adhesion preserves eye patterning as axonal retinotopy in the *Drosophila* brain, Current Biology (2026), https://doi.org/10.1016/j.cub.2026.01.007

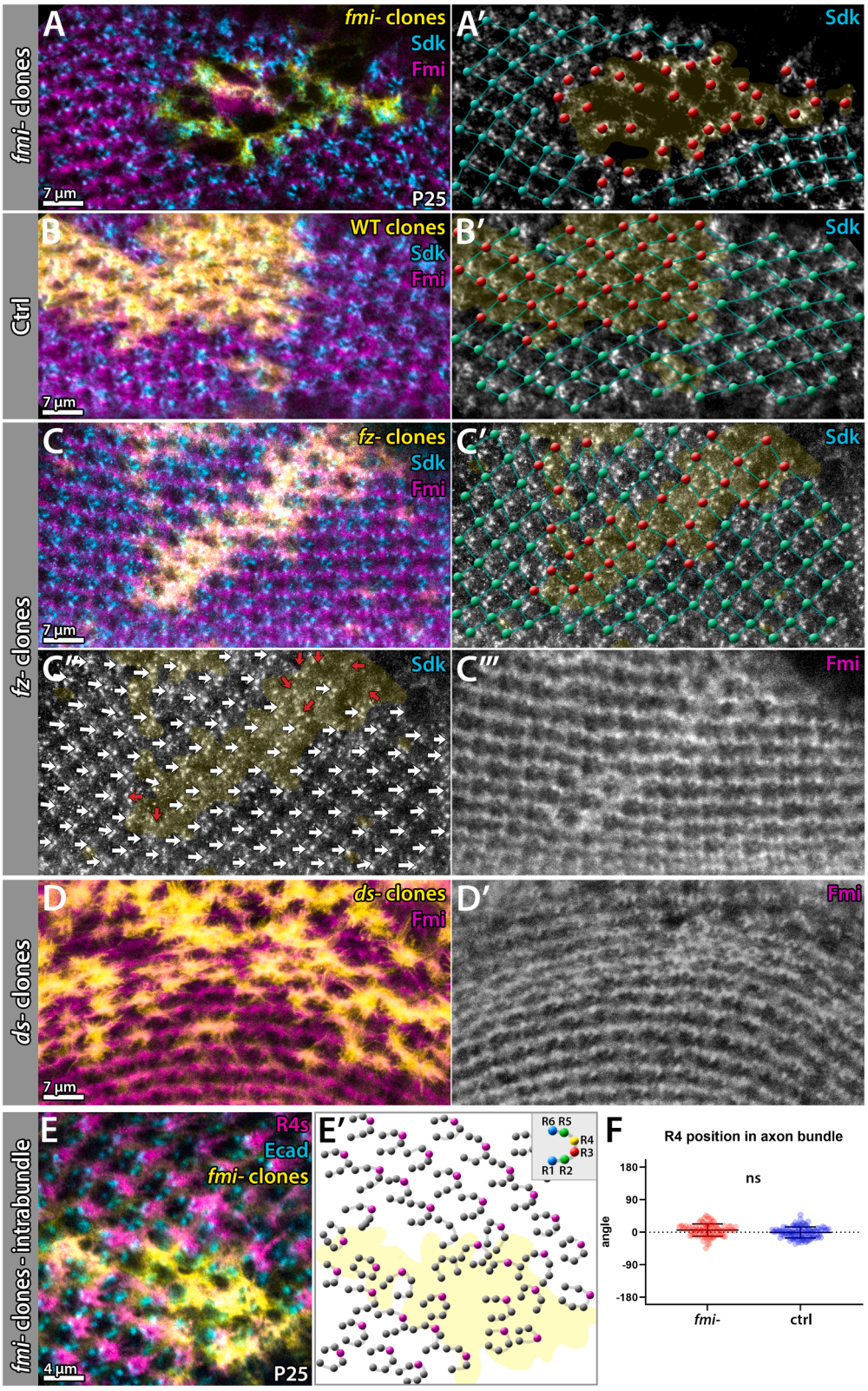

(legend on next page)

Please cite this article in press as: Kehribar et al., Selective adhesion preserves eye patterning as axonal retinotopy in the *Drosophila* brain, Current Biology (2026), https://doi.org/10.1016/j.cub.2026.01.007

We analyzed the effect of loss of *sdk* on the integrity of axon bundles above the lamina plexus. As shown in Figures 5B and S5C and Video S3, individual mutant axons left their "home" bundles and re-attached to other bundles. Tracing of individual axons in the *sdk* mutant revealed braiding, i.e., axons switching positions within a bundle, that are never observed in wild type (Figures 5B, S5A, S5B, and S5D). The intra-bundle braiding defects in the *sdk* mutant contrast with the *fmi* mutant, which exhibited no braiding within bundles (Figures S5D–S5F). Furthermore, analysis of the lamina plexus revealed that loss of *sdk* leads to variable numbers of axon terminals per bundle and positions of the R4 subtype (Figures 5E–5H). In wild type as well as in the otherwise (inter-bundle) disorganized lamina plexus formed by *fmi* mutant growth cones (cf. Figures 4E and 4F), R4 occupies a single, stereotypic position in each bundle (Figures 5F–5F″). By contrast, in the *sdk* mutant, R4s were heterogeneously distributed, with many bundles lacking an R4 and others containing more than one (Figures 5E–5F″), while cell body organization in the eye remained intact (Figures 5G, 5H, S6K, and S6L).

If individual R1–6 axons, including single R2s and R5s, can detach from their ommatidial bundles and re-attach elsewhere (Figures 5A, 5B, S5B, and S5C), then inter-bundle organization must also be disrupted in *sdk* mutants. This is evident when labeling R2/5-specific Fmi in the *sdk* mutant lamina plexus: the usual orthogonal pattern seen in controls (Figures 5I and S6M) was lost in the mutant (Figures 5J and S6N). Since our R2/5-driver also labels some R4s (arrowhead in S6M), we co-labeled R4 in a different color (STAR Methods). Fmi rings were found only around R2/5 heels (arrowhead in Figure S6N), not R4 (arrow in Figure S6N), confirming that Fmi accurately reflects R2/5 positions in the *sdk* mutant lamina plexus. We conclude that Sdk preserves intra-bundle axon adjacencies throughout the entire optic stalk.

Inter-bundle and intra-bundle adhesion synergistically ensure robustness of retinotopic patterning

Single R cell growth cones mutant for *fmi* appear indistinguishable from wild type in the lamina plexus.[45] We confirmed these observations in single cell clones for each of the six R1–6 subtypes (Figures S3A and S3B). Remarkably, single *sdk* mutant R1–6 growth cones also appear indistinguishable from wild type in a similar analysis (Figures S3C and S3D). Furthermore, neither single mutant causes the disintegration of the optic stalk or lamina plexus. However, partial structural breakdowns in the form of gaps in the lamina plexus have been reported in the *sdk* mutant in L3 larvae.[59] By contrast, we observed gaps in large *fmi* mutant clones, but not the *sdk* mutant, at P25 (Figures 4A and 4E).

To understand this discrepancy, we analyzed early lamina plexus development (Figures 6A and S6O). A top view of the lamina plexus in L3 larvae showed a highly heterogeneous structure with clusters and small gaps (Figures 6B and S6P). Clones of *fmi* null mutant axons exhibited both delayed arrival (cf. Figures 3I–3P) and larger gaps already at the L3 larval stage (Figures 6C, 6D, and S6Q). The *sdk* null mutant lamina plexus exhibited similar, albeit smaller, gaps (Figures 6E, 6F, S4K, S6U, and S6V). In both mutants we observed the phenotype of lamina cell bodies proximal of the lamina plexus, as previously reported for *sdk*[59] (arrowheads in Figures 6C and 6E). Combining *fmi* RNAi in all R cells, which has milder defects than the *fmi* null mutant (Figures S6Q–S6T; defects became apparent at P25; Figure 6J), and the *sdk* null mutant led to a complete loss of discernible structure (Figures 6G, 6H, S6W, and S6X).

At P25, the wild-type lamina plexus has patterned into a precise, gap-free lattice (Figure 6I). As shown above, small *fmi* null mutant clones could recover due to the delayed arrival of axons (Figures 3I–3P), while large *fmi* null mutant clones retained gaps (Figures 4A and 4E). The milder phenotypes obtained with *fmi* RNAi include pattern disruptions but no gaps (Figure 6J). The *sdk* null mutant lamina plexus had a very different phenotype, with only small gaps, but an apparent randomization of the R cell lattice not seen in *fmi* (Figure 6K; compare also Figure 5J). *fmi* RNAi in the *sdk* mutant background led to remnants of the lamina plexus with an almost complete loss of discernible structure (Figure 6L). A consistent progression of these phenotypes was observed at P40 (Figures 6M–6P) and during lamina column formation at P50 (Figures 6Q–6T). The structural integrity of the "randomized" *sdk* mutant lamina plexus was maintained at P40 and lamina formation at P50 (Figures 6O and 6S). We conclude that both *fmi* and *sdk* mutants exhibit early gaps, which can resolve to different degrees. While large *fmi* clones retain gaps, loss of *sdk* in the entire lamina plexus by P25 allows for a stable, largely gap-free growth cone sheet with randomized R cell terminals.

Loss of both *fmi* and *sdk* led to a loss of structural integrity of the lamina plexus, including clusters of axons that remained stalled above the lamina plexus at late developmental stages (P40; compare arrows in Figure 6P with Figures 6M–6O) and even after cartridge formation at P50 (Figure 6Q–6T). This phenotype is reminiscent of the delayed single *fmi* mutant R cell axons that could still be "pulled in" during subsequent development. This correction did not occur in the double mutant, suggesting that delayed *fmi* mutant R2/5 axons were eventually integrated via their intra-bundle Sdk adhesion. Hence, even though both cell adhesion molecules have distinct and complementary functions, the way the adhesive forces work together appears partially redundant from a genetics perspective. These findings suggest that the two types of selective adhesion in the correct spatiotemporal pattern synergistically ensure robustness of precise pattern formation of axonal interactions.

Figure 4. Fmi is required for inter-bundle, but not intra-bundle adhesion independent of known signaling functions

(A and B) Large *fmi*− clones (yellow; A) disrupt inter-bundle patterning in the lamina plexus (A′). Wild-type clone as control in (B). $n = 15$ each.

(C and D) *fz*− and *ds*− clones leave the inter-bundle patterning intact (yellow; C′ and D) and do not affect Fmi levels (C‴ and D′). Rotational defects can be observed in *fz*− regions (red arrows in C″), which affect the Fmi pattern (C‴). $n = 12$ and 5, respectively.

(E and F) Intra-bundle patterning is intact in *fmi*− regions (yellow), based on the stereotypic position of R4s (magenta) in the bundle (top right corner in E′). R4 position can be identified using E-cadherin staining (cyan). Quantification shows R4 positions similar to control (F). Error bars represent SD; lines represent mean. $n = 6$ optic lobes, 86 *fmi*− R4s, 101 control R4s. Stage P25 for all images.

See also Figures S3 and S4 and Table S1.

Please cite this article in press as: Kehribar et al., Selective adhesion preserves eye patterning as axonal retinotopy in the *Drosophila* brain, Current Biology (2026), https://doi.org/10.1016/j.cub.2026.01.007

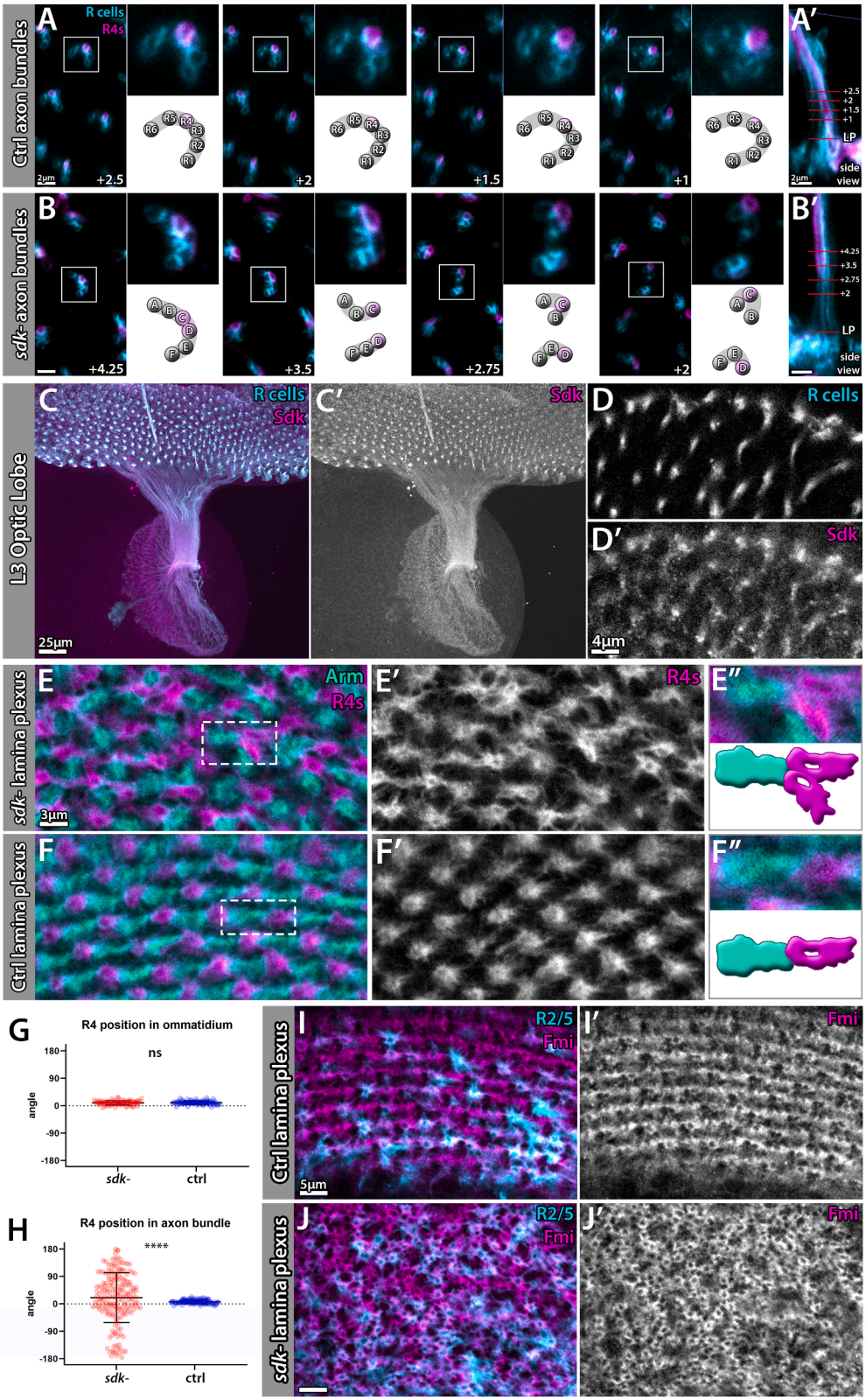

(legend on next page)

Please cite this article in press as: Kehribar et al., Selective adhesion preserves eye patterning as axonal retinotopy in the *Drosophila* brain, Current Biology (2026), https://doi.org/10.1016/j.cub.2026.01.007

A computational model of row-by-row arrival of R cell axon terminals in time generates the retinotopic pattern, including the shape of the postsynaptic lamina neurons

The two selective adhesive mechanisms suggest a model for interactions among axonal rows in time that re-establish the eye pattern as retinotopic pattern in the brain. First, rows of R2/5 (and R8) axons, held together by Fmi interaction, are wrapped around the optic stalk (Figure 7A); next, the youngest row of R2/5s could be attached to the next older row through Fmi in a zipper-like fashion (Figure 7B). At the same time, R3/4 intercalate in older rows, held in place by Sdk interactions (Figure 7B, oldest row), followed by R1/6 intercalation and a corresponding expansion of the lamina plexus. To test whether these two forces are sufficient to recreate the pattern in the lamina plexus in a row-by-row fashion in time we turned to computational modeling.

First, we simulated the two selective adhesive mechanisms as atomic forces, where the axon terminals are treated as "atoms" that interact via circular potentials. A simulation of Fmi and Sdk adhesion allowed the row-by-row addition of R cell axons in a stable pattern (Figure 7C; Video S4). However, this approach failed to simulate the growth and expansion of the lamina plexus, which arises from the continued intercalation of R3/4s and R1/6s into the existing R2/5 scaffold. Including growth in the atom model led to shifts along the boundaries of the circular potentials that result from a lack of extended and flexible membrane-to-membrane contact areas for Fmi and Sdk adhesion. Hence, physical properties of the axon terminals and especially extended adhesive interfaces may be an important part of the mechanism that allows the row-by-row growth.

To implement axon terminals with flexible physical shapes and adhesive interfaces, we used the Unity game engine, known for the interactive simulation of dynamic, physical objects that interact through defined forces in video games (think "Angry Birds" of visual map formation). Each axon terminal was simulated as a "soft body" with noisy interaction dynamics (STAR Methods). We simulated the patterned appearance of R cell growth cones as before: first, rows of R8s and surrounding R2/5s appear in a zigzag pattern (Video S5; Figure 7D). All R8/2/5s interact with equal forces (Flamingo, marked in blue in Figure 7D; R8 not shown) and thereby preserve the inter-bundle axonal pattern imposed by the R2/5 cell bodies of neighboring ommatidia in the developing eye. As each new R2/5 row appears and integrates on the anterior edge based on the same Flamingo interaction, a row of R3/4s appears in the posterior, i.e., older row of R2/5s (Video S5; Figure 7E). R3/4s, followed by R1/6, integrate based on intra-bundle (Sdk) adhesion between R2 and R5 (Figure 7F). Note that this mechanism allows for simple swapping of the R3/4 and R1/6 sides of the R2/5 axis on the other side of the equator (see below).

We simulated the intra-bundle force (Sidekick) as practically "unbreakable." By contrast, the inter-bundle force (Flamingo) must yield to the integration of R3/4 and later R1/R6 and their intercalation in the initial grid formed by R2/5s (Figures 7B and 7E for R3/4 intercalation). Specifically, when R3/4s and R1/6s appear, the "early Flamingo" between all R2/5s is replaced with an inter-bundle force to intercalate the new axon terminals to form R1-R2-R6-R5-R1-etc. rows based on our experimental observations at P25 (numbers and blue Fmi connections marked in Figure 7F). The growing structure recapitulates the pattern of the wild-type lamina plexus (Video S5; Figure 7F). As the pattern grows, it also generates a pattern of gaps in the R1–6 scaffold exactly where all target L cells are located in the wild-type structure, even though the L cells are not included in the simulation (Figures 7F and 7G). These "non-R cell" spaces have a shape that appears highly similar to the non-trivial biological shape of L cell neurites observed in the lamina plexus (compare Figures 7F′ and 7G′). Three quantitative measures of shape similarity (including "Hu moments"; STAR Methods) revealed a highly significant similarity when compared to random shapes of similar attributes (Figures S7A–S7C). This surprising outcome indicates that the shape of L cell neurites may entirely be determined by the surrounding R cell axons, consistent with our previous finding that L cells serve no active role during this phase of development.[7] While the computational model creates the shape of L cells when allowed to contain non-R cell space in the growing lattice, the actual ablation of all L cells[7] leads to a space-filling circular arrangement of R cell growth cones. We therefore repeated our simulation without allowing large non-R cell spaces and recapitulated the published biological outcome (STAR Methods; Figure S7D; Video S6). Hence, our growth model based on inter- and intra-bundle R cell adhesion can generate both the biologically observed retinotopic map when L cells are ablated, as well as the shape of L shapes if actual L cells are present to fill this space.

A statistical analysis of 100 simulations reveals the robustness of the pattern generated through the row-by-row growth process (Figure 7H). The pattern variability appears similar to that observed in the biological sample, while the relative positioning of all R1–6 axons in the correct retinotopic pattern is preserved throughout. The precision of the pattern remains stable with each subsequent row (Figure 7I). This robustness further holds for a simulation of the equator region, where a mirror-symmetric density of R3/4 axon terminals changes the pattern (Video S5; Figures 7J–7L). Note that intra-row Fmi adhesion across the

Figure 5. The R1–6 intra-bundle organization is preserved through the homophilic cell adhesion molecule Sidekick

(A and B) Control axons (cyan) maintain adjacencies throughout the length of the axon shaft, with R4s (magenta) occupying their stereotypical position inside the bundle. *sdk*− axon bundles (B) lose integrity through braiding, with R4s occupying random positions in the bundle. Single frames from (A) and (B) taken from axon bundles shown as red lines in (A′) and (B′). Stage P33; $n = 3$ and 4, respectively.

(C and D) Sdk (magenta) is expressed equally on all axon bundles (cyan) in the L3 optic stalk. $n = 6$.

(E–H) At P25, R4s (magenta) are randomly positioned in the *sdk*− lamina plexus. Bundles marked by Arm-positive L cells (cyan) contain either more or less than one R4 (E″ and F″). $n = 12$ and 2, respectively. R4 position is only affected in the lamina plexus, not the retina (G and H). Error bars represent SD; lines represent mean. $p < 0.0001$. $n = 2$ optic lobes and 85 ommatidia, and 3 optic lobes and 92 ommatidia, respectively (G). $n = 3$ optic lobes and 192 bundles, and 3 optic lobes and 107 bundles, respectively (H).

(I and J) In contrast to the orthogonal pattern seen in a wild-type control (I), in the *sdk*− lamina plexus (J), R2/5s (cyan) occupy random positions, resulting in a randomized Fmi ring pattern (magenta). $n = 7$ and 22, respectively. Stage P25 (E–J).

See also Figures S3, S5, and S6; Table S1; and Video S3.

Please cite this article in press as: Kehribar et al., Selective adhesion preserves eye patterning as axonal retinotopy in the *Drosophila* brain, Current Biology (2026), https://doi.org/10.1016/j.cub.2026.01.007

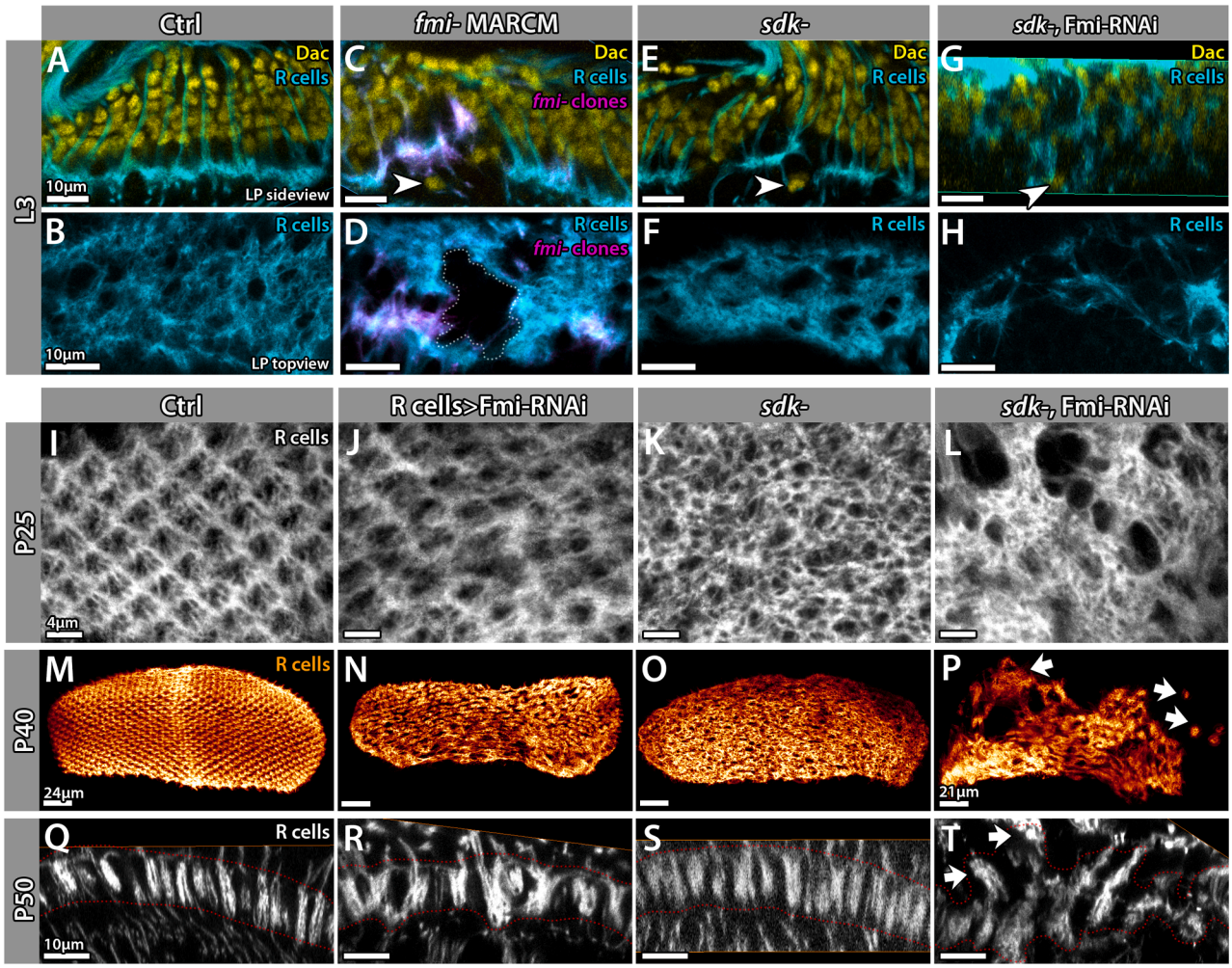

Figure 6. Inter-bundle and intra-bundle adhesion synergistically ensure robustness of retinotopic mapping

(A–H) Side views (A, C, E, and G) and top views (B, D, F, and H) of lamina plexi of wild-type control (A and B), *fmi*− (C and D), *sdk*− (E and F), and double-mutant (G and H) brains show varying degrees of disruption and holes at stage L3. L cells are mislocalized in all mutant cases (yellow; arrowheads). *n* = 8, 4, 10, and 12, respectively.

(I–L) At P25, lamina plexi of single mutants show inter- and intra-bundle defects, respectively (J and K); with no discernable pattern left in the double mutant (L). *n* = 15, 12, 31, and 12, respectively.

(M–P) At P40, compared to a wild-type control (M), defects in the lamina plexus can be observed in single mutants, but all axons are integrated (N and O). In the double mutant (P), axon bundles are still stalled above the lamina plexus (arrows). *n* = 11, 7, 10, and 10, respectively.

(Q–T) Side views of the lamina at P50 show that columns are positioned in the same plane (red dotted line) in a wild-type control (Q) and single mutants (R and S), whereas individual axons appear stalled outside the lamina in the double mutant (arrows in T). *n* = 15, 4, 23, and 12, respectively.

See also Figure S6 and Table S1.

equator of the initial R2/5 row is continuous (see Fmi marked in blue in Figure 7J). This "equator-blindness" of the initial R2/5 grid allows R3/4 vs. R1/6 to integrate on either side based on the same inter- and intra-bundle forces to generate a robust pattern in time.

Previous mutant analyses indicated that individual bundles that rotated up to 90 degrees (based on eye ommatidia rotations) likely ended up correctly integrated, whereas 180 degree rotations are rotated 180 degrees in the lamina plexus.[49] Correspondingly, in our computational growth model, a single bundle rotated up to 90 degrees was robustly corrected in the lamina plexus (Figures S7E–S7G), while a 180 degree rotated bundle was stabilized in the flipped position (Figure 7M). Hence, the model recapitulates and explains the earlier experimental findings of bundle rotations in the lamina plexus.

Last, we simulated retinotopic map formation in the absence of the inter-bundle force (*fmi* mutant), the absence of the intra-bundle force (*sdk* mutant), and in a simulated double mutant. The starting points of these simulations reflect the defects resulting from axonal misorganization in the optic stalk: for the starting point of the *fmi* simulation, we rotated R2/5 randomly but spawned R3/4 and R1/6 in their correct relative positions. In the *sdk* simulation we spawned R2/5 correctly (although this is likely also disrupted in biology), but noise was added to the spawning position of R1/6 and R3/4. In the simulated double mutant, all R cell axons can spawn in a wrong position, and

Please cite this article in press as: Kehribar et al., Selective adhesion preserves eye patterning as axonal retinotopy in the *Drosophila* brain, Current Biology (2026), https://doi.org/10.1016/j.cub.2026.01.007

CellPress
OPEN ACCESS

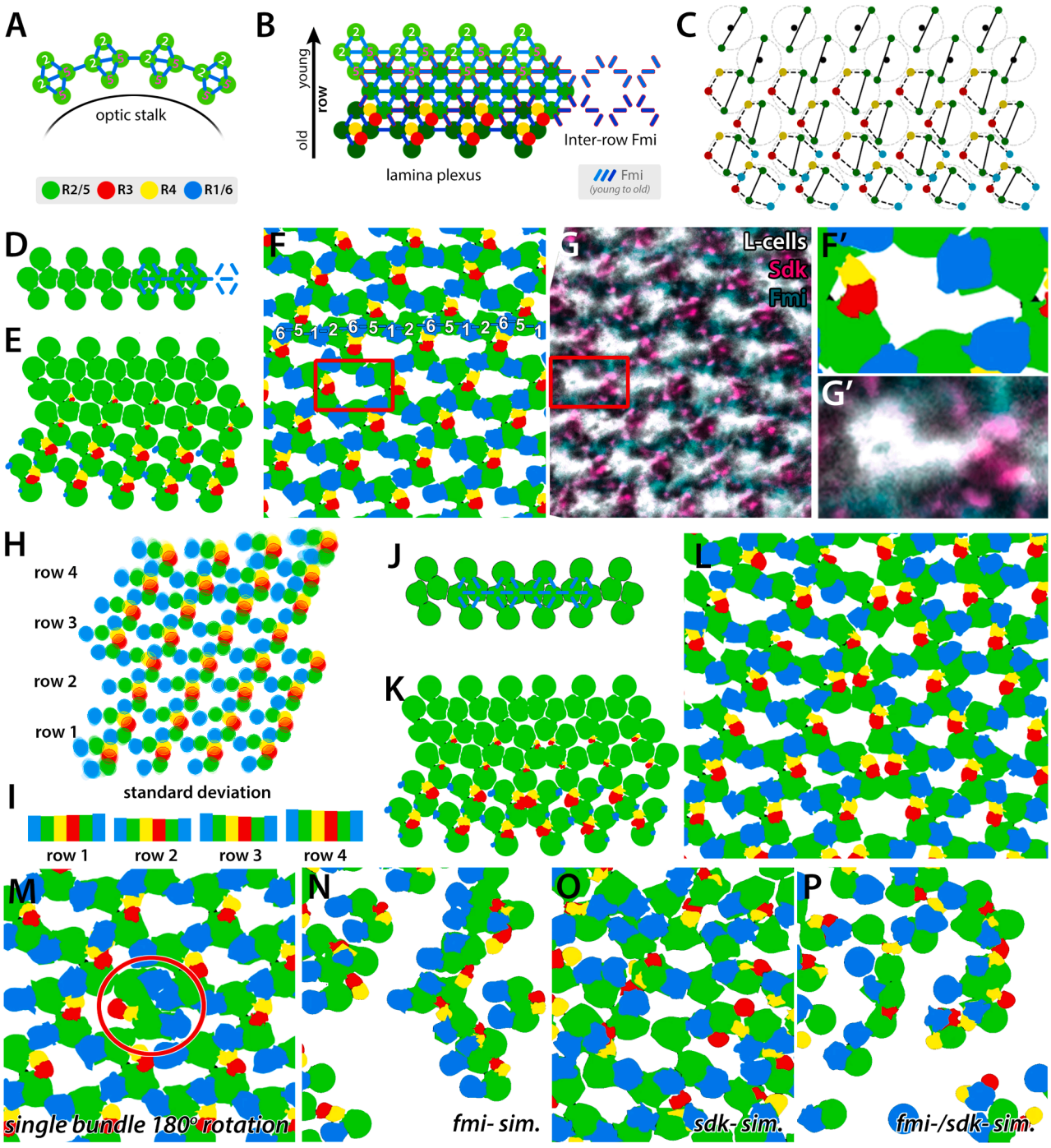

Figure 7. A computational model of row-by-row arrival of R cell axon terminals in time generates the retinotopic pattern, including the shape of the postsynaptic lamina neurons

(A and B) Rows of R2/5 axons, held together by Fmi (blue), wrap around the optic stalk (A). The youngest row attaches to the next oldest row through Fmi in the lamina plexus (B).

(C) "Atom model" simulation of the retinotopic mapping in the lamina plexus.

(D) "Soft body model," rows of R2/5s appear in a zigzag pattern, interconnected through Fmi (blue).

(E) As each new R2/5 row appears and integrates on the anterior edge based on the same Fmi interaction, a row of R3/4s appears in the posterior, i.e., older row of R2/5s.

(F and G) Outcome of soft body model simulation. Initial Fmi between R2/5s is replaced with R1/6s that intercalate in the final pattern (F; one row labeled with R cell numbers). Inset highlights the shape of "empty" space generated by R cells, which matches the shape of L cells in the biological structure (white in G).

(legend continued on next page)

Please cite this article in press as: Kehribar et al., Selective adhesion preserves eye patterning as axonal retinotopy in the *Drosophila* brain, Current Biology (2026), https://doi.org/10.1016/j.cub.2026.01.007

bundles can be rotated (Video S7). The three mutant simulations recapitulate the biological phenotypes well, including the large gaps in the *fmi* mutant, while the *sdk* mutant lamina plexus appears randomly shuffled, while maintaining its structural integrity without large gaps. More conservative simulations with a lack of *fmi* and *sdk* adhesion only after a hypothetical initially correct row-by-row arrival revealed similar but milder mutant-specific defects (Figures S7H–S7J; Video S7). In sum, all *in silico* experiments recapitulate—and provide mechanistic explanations for—the experimental observations reported in this study.

DISCUSSION

We have characterized a mechanism for the development of retinotopic axonal projections in the *Drosophila* brain that is solely based on axon-axon interactions of photoreceptor neurons. The target-independent self-organization of axon terminals is embedded in a larger developmental program that ultimately ensures a functional neural network in the outcome. First, the sheet of growth cones forms between two layers of glial cells that ensure its precise localization.[60,61] Second, as the axons grow, their interactions with glia cells are required for the differentiation of the target L cells, which thereby send their neurites at the exact right time and place to be intercalated in the retinotopic map.[62] Hence, the "mapping mechanism" can only be understood as a series of interdependent steps in time.

In trying to reduce the description of retinotopic map formation to a minimal set of molecular and cellular mechanisms, we identified three factors: (1) the cellular temporal gradient as an organizing principle based on preceding eye development, (2) selective molecular adhesion with spatiotemporal specificity, and (3) physical properties of the axon terminals with flexible adhesive surfaces to shape the morphology of the retinotopically patterned sheet of growth cones in the brain.

Temporal gradients have been found to be critical for retinotopic map formation across species. In vertebrates, both the retinal ganglion cells as well as their target structures develop in temporal waves.[61,63–65] In addition, in vertebrates, molecular gradients are a core mechanism to guide the patterned arrival of axons in the right target regions.[3,4,6,63,66–72] While it has been suggested that under certain conditions molecular gradients can serve as a precise coordinate system,[73] several perturbation experiments have indicated that molecular gradients more commonly aid in relative positioning, i.e., the placement of incoming axons next to the preceding neighbor in time. Notably, bilateral ablation of the tectum, the main target region of retinotopic projections of retinal gangling cells in fish, results in the formation of a retinotopic axonal projections in an incorrect brain region,[74] similar to our observations in flies.[7] We conclude that temporally patterned axonal growth is a powerful organization principle, but only if further factors, most notably selective molecular adhesion, ensure axonal pattern preservation.

The role of selective adhesion in axon-axon interactions during the temporally patterned growth of retinotopic projections was recognized already in the 1980s, based on experiments with the chick retina as a model.[8] Since then, several studies in vertebrates have demonstrated the critical role of axon-axon interactions in topographic map formation.[13,14] For *Drosophila*, we here identified early developmental roles for the cell adhesion molecules Fmi and Sdk in preserving the photoreceptor cell body pattern as axonal projections in the brain through two independent mechanisms. We note that Fmi is exquisitely adapted for a mechanical, tension-based breaking and intercalation process. Fmi is an adhesion GPCR and interacts homophilically across cell-cell contacts via its elaborate extracellular domain. Recent structural studies have shown that the mouse Fmi homolog CELSR1 can form flexible antiparallel dimers that may bridge distances between 500–600 Å.[75] Intercalation through Fmi dimer separation may occur through an increase in force amplitude or angle.[76–78]

The importance to identify the earliest phenotypes in *fmi* and *sdk* mutants is highlighted by our findings that *fmi*− axons initially show stalling defects that are corrected during subsequent development, potentially through Sdk-mediated intra-bundle adhesion. Similarly, *sdk* mutants exhibit defects in lamina plexus integrity in larval stages that appear corrected in later developmental stages. Our characterization of the earliest discernible defects in the mutant optic stalk does not exclude additional functions for either molecule during later developmental processes, as reported in previous studies.[59,79,80] Yet the early roles in preserving the eye pattern through selective adhesion differ from traditional interpretations of axonal target guidance and are more reminiscent of the classical 1970 proposal of the differential adhesion hypothesis by Steinberg.[81,82] Critically, the differential adhesion hypothesis was formulated to explain self-assembly and an equilibrium configuration of cells based on selective adhesion and physical properties, especially surface tension.[81]

The physical properties of retinal axon terminals are not easily experimentally accessible, but their dynamic shape and extensions have been described in detail based on high-resolution live imaging.[7,17] We therefore simulated the physical properties, i.e., physical extension, surface tension and deformation through physical interactions and adhesion on the surfaces of soft bodies. This minimal set of physical properties apparent in the biological structure, together with the temporal row-by-row growth and the two selective adhesive forces, produced a remarkable morphological mimic of the lamina plexus. Unexpectedly, the growth purely based on retinal axon interaction rules produced not only the spaces where the future postsynaptic L cell dendrites are located but also their precise, non-trivial shape. This suggests that the morphogenesis of L cell shape at

(H and I) Statistical analysis of 100 simulations reveals the robustness of the pattern generated through the row-by-row growth process (H). The precision of the pattern, as measured by the standard deviation (I), remains stable with each subsequent row.
(J–M) The simulated adhesive forces generate the same retinotopic mapping, even across an equator region. (J) R2/5s can form stable rows based on inter-bundle Flamingo (blue bars). Addition of R3/4s (red/yellow) and R1/6 (blue) based on Sidekick adhesion maintains the equator (K). (L) The final pattern is contiguous across the equator. (M) A single 180-degree rotated bundle integrates stably in the pattern.
(N–P) Simulations of *fmi*− (N), *sdk*− (O), and *fmi*−;*sdk*− (P) conditions replicate phenotypes in biological samples.
See also Figure S7; Table S1; and Videos S4, S5, S6, and S7.

this developmental stage is passive and determined by the actively patterning retinal axons. Later during development, L cells become active agents, first in the stabilization of R cell growth cone fronts to ensure neural superposition[7] and subsequently in the morphogenesis of lamina columns.[83]

We conclude that a minimal set of contributing factors is required to satisfactorily explain axonal retinotopic patterning in the fly brain as a composite instruction in time,[84] including (1) a temporal gradient imposed by preceding eye development, (2) preservation of spatial organization through selective adhesion, and (3) morphogenesis of a sheet of axon terminals based on physical interaction properties and surface tension, as proposed by the original differential adhesion hypothesis.

RESOURCE AVAILABILITY

Lead contact

Requests for further information and resources should be directed to and will be fulfilled by the lead contact, P. Robin Hiesinger (robin.hiesinger@fu-berlin.de).

Materials availability

All fly lines generated in this study are available from the lead contact upon request.

Data and code availability

- All original microscopy and statistical data reported in this study are available from the lead contact upon request.
- Custom codes for simulating retinotopy are freely available through GitHub (https://github.com/KleistLab/Retinotopy) and a frozen version (V.0.1) to generate the images in Figure 7 as well as Videos S4, S5, S6, and S7 are available through Zenodo https://doi.org/10.5281/zenodo.15561406.
- Any additional information required to reanalyze the data reported in this paper is available from the lead contact upon request.

ACKNOWLEDGMENTS

We thank all members of the Hiesinger lab for helpful discussions and Gerit Linneweber, Randolf Menzel, and Tobias Langenhan for comments on the manuscript. We would also like to thank D. Strutt, G. Struhl, and T. Langenhan for generously sharing reagents. This work was supported by DFG Research Unit 5289 *RobustCircuit* project Z1 (453877723; to M.v.K. and P.R.H.), DFG grant number 450430223 to M.v.K. and P.R.H., and funding from the European Research Council (ERC) under the European Union's Horizon 2020 research and innovation programme (grant agreement no. 101019191 to P.R.H.).

AUTHOR CONTRIBUTIONS

M.K., C.B.W., and P.R.H. conceived the study and wrote the paper. All authors gave feedback on the manuscript. M.K., C.B.W., N.W., and E.A. performed all biological experiments. K.K., E.T.R., and M.v.K. performed all computational modeling experiments. L.Q.W. provided assistance with visualization and created the animations in the video abstract.

DECLARATION OF INTERESTS

The authors declare no competing interests.

STAR★METHODS

Detailed methods are provided in the online version of this paper and include the following:

- KEY RESOURCES TABLE
- EXPERIMENTAL MODEL AND STUDY PARTICIPANT DETAILS
  - Fly husbandry and genetics
- METHOD DETAILS
  - Histology and fixed imaging
  - Antibody screening
  - Ex-vivo brain cultures
  - 2-photon intravital live imaging
  - Expansion microscopy
  - Endogenous Fmi-mCherry-pHluorin knock-in
  - Computational modeling – atom model
  - Computational modeling – soft body model
  - Animation of retinotopic map formation
- QUANTIFICATION AND STATISTICAL ANALYSIS
  - Equator analysis
  - Quantification of correlation between Fmi and R cell subtypes
  - *fmi-* axon arrival analysis
  - Bundle distance analysis
  - Intrabundle R4 position analysis in the lamina plexus
  - Braiding analysis
  - Identifying inter-bundle pattern in *sdk* mutants
  - Fmi-mCherry-pHluorin levels in the lamina plexus
  - Quantification and data analysis
  - Quantification of L cell shapes in computational model and biological data
  - Statistical analysis

SUPPLEMENTAL INFORMATION

Supplemental information can be found online at https://doi.org/10.1016/j.cub.2026.01.007.

A video abstract is available at https://doi.org/10.1016/j.cub.2026.01.007#mmc10.

Received: November 13, 2025
Revised: December 4, 2025
Accepted: January 7, 2026

REFERENCES

1. Clandinin, T.R., and Feldheim, D.A. (2009). Making a visual map: mechanisms and molecules. Curr. Opin. Neurobiol. *19*, 174–180. https://doi.org/10.1016/j.conb.2009.04.011.
2. McLaughlin, T., and O'Leary, D.D.M. (2005). Molecular gradients and development of retinotopic maps. Annu. Rev. Neurosci. *28*, 327–355. https://doi.org/10.1146/annurev.neuro.28.061604.135714.
3. Cheng, H.J., Nakamoto, M., Bergemann, A.D., and Flanagan, J.G. (1995). Complementary gradients in expression and binding of ELF-1 and Mek4 in development of the topographic retinotectal projection map. Cell *82*, 371–381. https://doi.org/10.1016/0092-8674(95)90426-3.
4. Drescher, U., Kremoser, C., Handwerker, C., Löschinger, J., Noda, M., and Bonhoeffer, F. (1995). In vitro guidance of retinal ganglion cell axons by RAGS, a 25 kDa tectal protein related to ligands for Eph receptor tyrosine kinases. Cell *82*, 359–370. https://doi.org/10.1016/0092-8674(95)90425-5.
5. Triplett, J.W. (2014). Molecular guidance of retinotopic map development in the midbrain. Curr. Opin. Neurobiol. *24*, 7–12. https://doi.org/10.1016/j.conb.2013.07.006.
6. Malin, J., and Desplan, C. (2021). Neural specification, targeting, and circuit formation during visual system assembly. Proc. Natl. Acad. Sci. USA *118*, e2101823118. https://doi.org/10.1073/pnas.2101823118.
7. Agi, E., Reifenstein, E.T., Wit, C., Schneider, T., Kauer, M., Kehribar, M., Kulkarni, A., von Kleist, M., and Hiesinger, P.R. (2024). Axonal self-sorting without target guidance in Drosophila visual map formation. Science *383*, 1084–1092. https://doi.org/10.1126/science.adk3043.

8. Bonhoeffer, F., and Huf, J. (1985). Position-dependent properties of retinal axons and their growth cones. Nature *315*, 409–410. https://doi.org/10.1038/315409a0.

9. Bonhoeffer, F., and Huf, J. (1980). Recognition of cell types by axonal growth cones in vitro. Nature *288*, 162–164. https://doi.org/10.1038/288162a0.

10. Cang, J., and Feldheim, D.A. (2013). Developmental mechanisms of topographic map formation and alignment. Annu. Rev. Neurosci. *36*, 51–77. https://doi.org/10.1146/annurev-neuro-062012-170341.

11. Petrovic, M., and Schmucker, D. (2015). Axonal wiring in neural development: Target-independent mechanisms help to establish precision and complexity. BioEssays *37*, 996–1004. https://doi.org/10.1002/bies.201400222.

12. Agi, E., Kulkarni, A., and Hiesinger, P.R. (2020). Neuronal strategies for meeting the right partner during brain wiring. Curr. Opin. Neurobiol. *63*, 1–8. https://doi.org/10.1016/j.conb.2020.01.002.

13. Cioni, J.M., Wong, H.H.W., Bressan, D., Kodama, L., Harris, W.A., and Holt, C.E. (2018). Axon-axon interactions regulate topographic optic tract sorting via CYFIP2-dependent WAVE complex function. Neuron *97*, 1078–1093.e6. https://doi.org/10.1016/j.neuron.2018.01.027.

14. Imai, T., Yamazaki, T., Kobayakawa, R., Kobayakawa, K., Abe, T., Suzuki, M., and Sakano, H. (2009). Pre-target axon sorting establishes the neural map topography. Science *325*, 585–590. https://doi.org/10.1126/science.1173596.

15. Braitenberg, V. (1967). Patterns of projection in the visual system of the fly. I. Retina-lamina projections. Exp. Brain Res. *3*, 271–298. https://doi.org/10.1007/BF00235589.

16. Kirschfeld, K. (1967). The projection of the optical environment on the screen of the rhabdomere in the compound eye of the Musca. Exp. Brain Res. *3*, 248–270. https://doi.org/10.1007/BF00235588.

17. Langen, M., Agi, E., Altschuler, D.J., Wu, L.F., Altschuler, S.J., and Hiesinger, P.R. (2015). The developmental rules of neural superposition in Drosophila. Cell *162*, 120–133. https://doi.org/10.1016/j.cell.2015.05.055.

18. Horder, T.J., and Martin, K.A. (1978). Morphogenetics as an alternative to chemospecificity in the formation of nerve connections. A review of literature, before 1978, concerning the control of growth of regenerating optic nerve fibres to specific locations in the optic tectum and a new interpretation based on contact guidance. Symp. Soc. Exp. Biol. *32*, 275–358.

19. Sato, M., Suzuki, T., and Nakai, Y. (2013). Waves of differentiation in the fly visual system. Dev. Biol. *380*, 1–11. https://doi.org/10.1016/j.ydbio.2013.04.007.

20. Kulkarni, A., Ertekin, D., Lee, C.H., and Hummel, T. (2016). Birth order dependent growth cone segregation determines synaptic layer identity in the Drosophila visual system. eLife *5*, e13715. https://doi.org/10.7554/eLife.13715.

21. Meinertzhagen, I.A. (1973). Development of the compound eye and optic lobe of insects. In Developmental Neurobiology of Arthropods, D. Young, ed. (Cambridge University Press; American Branch), p. 268.

22. Wolff, T., and Ready, D.F. (1993). Pattern formation in the Drosophila retina. In The Development of Drosophila melanogaster (Cold Spring Harbor Laboratory Press), pp. 1277–1325.

23. Wolff, T., and Ready, D.F. (1991). The beginning of pattern formation in the Drosophila compound eye: the morphogenetic furrow and the second mitotic wave. Development *113*, 841–850. https://doi.org/10.1242/dev.113.3.841.

24. Tomlinson, A., and Ready, D.F. (1987). Neuronal differentiation in Drosophila ommatidium. Dev. Biol. *120*, 366–376. https://doi.org/10.1016/0012-1606(87)90239-9.

25. Ready, D.F., Hanson, T.E., and Benzer, S. (1976). Development of the Drosophila retina, a neurocrystalline lattice. Dev. Biol. *53*, 217–240. https://doi.org/10.1016/0012-1606(76)90225-6.

26. Kumar, J.P. (2011). My what big eyes you have: how the Drosophila retina grows. Dev. Neurobiol. *71*, 1133–1152. https://doi.org/10.1002/dneu.20921.

27. Strutt, H., and Strutt, D. (2021). How do the Fat-Dachsous and core planar polarity pathways act together and independently to coordinate polarized cell behaviours? Open Biol. *11*, 200356. https://doi.org/10.1098/rsob.200356.

28. Cooper, M.T., and Bray, S.J. (1999). Frizzled regulation of Notch signalling polarizes cell fate in the Drosophila eye. Nature *397*, 526–530. https://doi.org/10.1038/17395.

29. Fanto, M., and Mlodzik, M. (1999). Asymmetric Notch activation specifies photoreceptors R3 and R4 and planar polarity in the Drosophila eye. Nature *397*, 523–526. https://doi.org/10.1038/17389.

30. Bollepogu Raja, K.K., Yeung, K., Shim, Y.K., Li, Y., Chen, R., and Mardon, G. (2023). A single cell genomics atlas of the Drosophila larval eye reveals distinct photoreceptor developmental timelines. Nat. Commun. *14*, 7205. https://doi.org/10.1038/s41467-023-43037-0.

31. Gallagher, K.D., Mani, M., and Carthew, R.W. (2022). Emergence of a geometric pattern of cell fates from tissue-scale mechanics in the eye. eLife *11*, 2.

32. Trujillo-Cenóz, O., and Melamed, J. (1966). Compound eye of dipterans: anatomical basis for integration–an electron microscope study. J. Ultrastruct. Res. *16*, 395–398. https://doi.org/10.1016/s0022-5320(66)80071-0.

33. Meinertzhagen, I.A.H., and T.E.. (1993). The development of the optic lobe. In The Development of Drosophila melanogaster.

34. Schwabe, T., Neuert, H., and Clandinin, T.R. (2013). A network of cadherin-mediated interactions polarizes growth cones to determine targeting specificity. Cell *154*, 351–364. https://doi.org/10.1016/j.cell.2013.06.011.

35. Struhl, G., Casal, J., and Lawrence, P.A. (2012). Dissecting the molecular bridges that mediate the function of Frizzled in planar cell polarity. Development *139*, 3665–3674. https://doi.org/10.1242/dev.083550.

36. Casal, J., Lawrence, P.A., and Struhl, G. (2006). Two separate molecular systems, Dachsous/Fat and Starry night/Frizzled, act independently to confer planar cell polarity. Development *133*, 4561–4572. https://doi.org/10.1242/dev.02641.

37. Das, G., Reynolds-Kenneally, J., and Mlodzik, M. (2002). The atypical cadherin Flamingo links Frizzled and Notch signaling in planar polarity establishment in the Drosophila eye. Dev. Cell *2*, 655–666. https://doi.org/10.1016/s1534-5807(02)00147-8.

38. Usui, T., Shima, Y., Shimada, Y., Hirano, S., Burgess, R.W., Schwarz, T.L., Takeichi, M., and Uemura, T. (1999). Flamingo, a seven-pass transmembrane cadherin, regulates planar cell polarity under the control of Frizzled. Cell *98*, 585–595. https://doi.org/10.1016/s0092-8674(00)80046-x.

39. Lee, R.C., Clandinin, T.R., Lee, C.H., Chen, P.L., Meinertzhagen, I.A., and Zipursky, S.L. (2003). The protocadherin Flamingo is required for axon target selection in the Drosophila visual system. Nat. Neurosci. *6*, 557–563. https://doi.org/10.1038/nn1063.

40. Umetsu, D., Murakami, S., Sato, M., and Tabata, T. (2006). The highly ordered assembly of retinal axons and their synaptic partners is regulated by Hedgehog/Single-minded in the Drosophila visual system. Development *133*, 791–800. https://doi.org/10.1242/dev.02253.

41. Kunes, S., Wilson, C., and Steller, H. (1993). Independent guidance of retinal axons in the developing visual system of Drosophila. J. Neurosci. *13*, 752–767. https://doi.org/10.1523/JNEUROSCI.13-02-00752.1993.

42. Chang, Y.C., Tsao, C.K., and Sun, Y.H. (2018). Temporal and spatial order of photoreceptor and glia projections into optic lobe in Drosophila. Sci. Rep. *8*, 12669. https://doi.org/10.1038/s41598-018-30415-8.

43. Williamson, W.R., Wang, D., Haberman, A.S., and Hiesinger, P.R. (2010). A dual function of V0-ATPase a1 provides an endolysosomal degradation mechanism in Drosophila melanogaster photoreceptors. J. Cell Biol. *189*, 885–899. https://doi.org/10.1083/jcb.201003062.

44. Jin, E.J., Kiral, F.R., Ozel, M.N., Burchardt, L.S., Osterland, M., Epstein, D., Wolfenberg, H., Prohaska, S., and Hiesinger, P.R. (2018). Live observation of two parallel membrane degradation pathways at axon terminals. Curr. Biol. *28*, 1027–1038.e4. https://doi.org/10.1016/j.cub.2018.02.032.

45. Chen, P.L., and Clandinin, T.R. (2008). The cadherin Flamingo mediates level-dependent interactions that guide photoreceptor target choice in Drosophila. Neuron *58*, 26–33. https://doi.org/10.1016/j.neuron.2008.01.007.

46. Chen, W.S., Antic, D., Matis, M., Logan, C.Y., Povelones, M., Anderson, G.A., Nusse, R., and Axelrod, J.D. (2008). Asymmetric homotypic interactions of the atypical cadherin flamingo mediate intercellular polarity signaling. Cell *133*, 1093–1105. https://doi.org/10.1016/j.cell.2008.04.048.

47. Bui, H.,D.L., Roach, A., Li, J., Bandekar, S.J., Orput, E., Raghavan, R., Arac, D., and Sando, R. (2023). The adhesion GPCRs CELSR1-3 and LPHN3 engage G proteins via distinct activation mechanisms. Preprint at bioRxiv. https://doi.org/10.1101/2023.04.02.535287.

48. Strutt, H., Warrington, S., Madathil, A.C.K., Langenhan, T., and Strutt, D. (2023). Molecular symmetry breaking in the Frizzled-dependent planar polarity pathway. Curr. Biol. *33*, 5340–5354.e6. https://doi.org/10.1016/j.cub.2023.10.071.

49. Clandinin, T.R., and Zipursky, S.L. (2000). Afferent growth cone interactions control synaptic specificity in the Drosophila visual system. Neuron *28*, 427–436. https://doi.org/10.1016/s0896-6273(00)00122-7.

50. Adler, P.N., Charlton, J., and Liu, J. (1998). Mutations in the cadherin superfamily member gene dachsous cause a tissue polarity phenotype by altering frizzled signaling. Development *125*, 959–968. https://doi.org/10.1242/dev.125.5.959.

51. Casal, J., Struhl, G., and Lawrence, P.A. (2002). Developmental compartments and planar polarity in Drosophila. Curr. Biol. *12*, 1189–1198. https://doi.org/10.1016/s0960-9822(02)00974-0.

52. Ma, D., Yang, C.H., McNeill, H., Simon, M.A., and Axelrod, J.D. (2003). Fidelity in planar cell polarity signalling. Nature *421*, 543–547. https://doi.org/10.1038/nature01366.

53. Rawls, A.S., Guinto, J.B., and Wolff, T. (2002). The cadherins fat and dachsous regulate dorsal/ventral signaling in the Drosophila eye. Curr. Biol. *12*, 1021–1026. https://doi.org/10.1016/s0960-9822(02)00893-x.

54. Strutt, H., and Strutt, D. (2002). Nonautonomous planar polarity patterning in Drosophila: dishevelled-independent functions of frizzled. Dev. Cell *3*, 851–863. https://doi.org/10.1016/s1534-5807(02)00363-5.

55. Yang, C.H., Axelrod, J.D., and Simon, M.A. (2002). Regulation of Frizzled by fat-like cadherins during planar polarity signaling in the Drosophila compound eye. Cell *108*, 675–688. https://doi.org/10.1016/s0092-8674(02)00658-x.

56. Eubelen, M., Bostaille, N., Cabochette, P., Gauquier, A., Tebabi, P., Dumitru, A.C., Koehler, M., Gut, P., Alsteens, D., Stainier, D.Y.R., et al. (2018). A molecular mechanism for Wnt ligand-specific signaling. Science *361*, eaat1178. https://doi.org/10.1126/science.aat1178.

57. Kimura, H., Usui, T., Tsubouchi, A., and Uemura, T. (2006). Potential dual molecular interaction of the Drosophila 7-pass transmembrane cadherin Flamingo in dendritic morphogenesis. J. Cell Sci. *119*, 1118–1129. https://doi.org/10.1242/jcs.02832.

58. Steimel, A., Wong, L., Najarro, E.H., Ackley, B.D., Garriga, G., and Hutter, H. (2010). The Flamingo ortholog FMI-1 controls pioneer-dependent navigation of follower axons in C. elegans. Development *137*, 3663–3673. https://doi.org/10.1242/dev.054320.

59. Astigarraga, S., Douthit, J., Tarnogorska, D., Creamer, M.S., Mano, O., Clark, D.A., Meinertzhagen, I.A., and Treisman, J.E. (2018). Drosophila Sidekick is required in developing photoreceptors to enable visual motion detection. Development *145*, dev158246. https://doi.org/10.1242/dev.158246.

60. Poeck, B., Fischer, S., Gunning, D., Zipursky, S.L., and Salecker, I. (2001). Glial cells mediate target layer selection of retinal axons in the developing visual system of Drosophila. Neuron *29*, 99–113. https://doi.org/10.1016/s0896-6273(01)00183-0.

61. Nakamura, H., and O'Leary, D.D. (1989). Inaccuracies in initial growth and arborization of chick retinotectal axons followed by course corrections and axon remodeling to develop topographic order. J. Neurosci. *9*, 3776–3795. https://doi.org/10.1523/JNEUROSCI.09-11-03776.1989.

62. Fernandes, V.M., Chen, Z., Rossi, A.M., Zipfel, J., and Desplan, C. (2017). Glia relay differentiation cues to coordinate neuronal development in Drosophila. Science *357*, 886–891. https://doi.org/10.1126/science.aan3174.

63. Hindges, R., McLaughlin, T., Genoud, N., Henkemeyer, M., and O'Leary, D.D.M. (2002). EphB forward signaling controls directional branch extension and arborization required for dorsal-ventral retinotopic mapping. Neuron *35*, 475–487. https://doi.org/10.1016/s0896-6273(02)00799-7.

64. Simon, D.K., and O'Leary, D.D. (1992). Development of topographic order in the mammalian retinocollicular projection. J. Neurosci. *12*, 1212–1232. https://doi.org/10.1523/JNEUROSCI.12-04-01212.1992.

65. Simon, D.K., and O'Leary, D.D. (1992). Influence of position along the medial-lateral axis of the superior colliculus on the topographic targeting and survival of retinal axons. Brain Res., Dev. Brain Res. *69*, 167–172. https://doi.org/10.1016/0165-3806(92)90155-p.

66. Feldheim, D.A., Kim, Y.I., Bergemann, A.D., Frisén, J., Barbacid, M., and Flanagan, J.G. (2000). Genetic analysis of ephrin-A2 and ephrin-A5 shows their requirement in multiple aspects of retinocollicular mapping. Neuron *25*, 563–574. https://doi.org/10.1016/s0896-6273(00)81060-0.

67. Monschau, B., Kremoser, C., Ohta, K., Tanaka, H., Kaneko, T., Yamada, T., Handwerker, C., Hornberger, M.R., Löschinger, J., Pasquale, E.B., et al. (1997). Shared and distinct functions of RAGS and ELF-1 in guiding retinal axons. EMBO J. *16*, 1258–1267. https://doi.org/10.1093/emboj/16.6.1258.

68. Nakamoto, M., Cheng, H.J., Friedman, G.C., McLaughlin, T., Hansen, M.J., Yoon, C.H., O'Leary, D.D., and Flanagan, J.G. (1996). Topographically specific effects of ELF-1 on retinal axon guidance in vitro and retinal axon mapping in vivo. Cell *86*, 755–766. https://doi.org/10.1016/s0092-8674(00)80150-6.

69. Frisén, J., Yates, P.A., McLaughlin, T., Friedman, G.C., O'Leary, D.D., and Barbacid, M. (1998). Ephrin-A5 (AL-1/RAGS) is essential for proper retinal axon guidance and topographic mapping in the mammalian visual system. Neuron *20*, 235–243. https://doi.org/10.1016/s0896-6273(00)80452-3.

70. Braisted, J.E., McLaughlin, T., Wang, H.U., Friedman, G.C., Anderson, D.J., and O'Leary, D.D. (1997). Graded and lamina-specific distributions of ligands of EphB receptor tyrosine kinases in the developing retinotectal system. Dev. Biol. *191*, 14–28. https://doi.org/10.1006/dbio.1997.8706.

71. McLaughlin, T., Hindges, R., and O'Leary, D.D.M. (2003). Regulation of axial patterning of the retina and its topographic mapping in the brain. Curr. Opin. Neurobiol. *13*, 57–69. https://doi.org/10.1016/s0959-4388(03)00014-x.

72. Nakamoto, T., Kain, K.H., and Ginsberg, M.H. (2004). Neurobiology: New connections between integrins and axon guidance. Curr. Biol. *14*, R121–R123. https://doi.org/10.1016/j.cub.2004.01.020.

73. Gosse, N.J., Nevin, L.M., and Baier, H. (2008). Retinotopic order in the absence of axon competition. Nature *452*, 892–895. https://doi.org/10.1038/nature06816.

74. Sharma, S.C. (1981). Retinal projection in a non-visual area after bilateral tectal ablation in goldfish. Nature *291*, 66–67. https://doi.org/10.1038/291066a0.

75. Bandekar, S.J., Garbett, K., Kordon, S.P., Dintzner, E.E., Li, J., Shearer, T., Sando, R.C., and Araç, D. (2025). Structural basis for regulation of CELSR1 by a compact module in its extracellular region. Nat. Commun. *16*, 3972. https://doi.org/10.1038/s41467-025-59319-8.

76. Fu, C., Huang, W., Tang, Q., Niu, M., Guo, S., Langenhan, T., Song, G., and Yan, J. (2023). Unveiling mechanical activation: GAIN domain unfolding

and dissociation in adhesion GPCRs. Nano Lett. *23*, 9179–9186. https://doi.org/10.1021/acs.nanolett.3c01163.

77. Scholz, N., Dahse, A.K., Kemkemer, M., Bormann, A., Auger, G.M., Vieira Contreras, F., Ernst, L.F., Staake, H., Körner, M.B., Buhlan, M., et al. (2023). Molecular sensing of mechano- and ligand-dependent adhesion GPCR dissociation. Nature *615*, 945–953. https://doi.org/10.1038/s41586-023-05802-5.
78. Zhong, B.L., Lee, C.E., Vachharajani, V.T., Bauer, M.S., Südhof, T.C., and Dunn, A.R. (2023). Piconewton forces mediate GAIN domain dissociation of the latrophilin-3 adhesion GPCR. Nano Lett. *23*, 9187–9194. https://doi.org/10.1021/acs.nanolett.3c03171.
79. Mann, K., Wang, M., Luu, S.H., Ohler, S., Hakeda-Suzuki, S., and Suzuki, T. (2012). A putative tyrosine phosphorylation site of the cell surface receptor Golden goal is involved in synaptic layer selection in the visual system. Development *139*, 760–771. https://doi.org/10.1242/dev.074104.
80. Takechi, H., Hakeda-Suzuki, S., Nitta, Y., Ishiwata, Y., Iwanaga, R., Sato, M., Sugie, A., and Suzuki, T. (2021). Glial insulin regulates cooperative or antagonistic Golden goal/Flamingo interactions during photoreceptor axon guidance. eLife *10*, e66718. https://doi.org/10.7554/eLife.66718.
81. Foty, R.A., and Steinberg, M.S. (2005). The differential adhesion hypothesis: a direct evaluation. Dev. Biol. *278*, 255–263. https://doi.org/10.1016/j.ydbio.2004.11.012.
82. Steinberg, M.S. (1970). Does differential adhesion govern self-assembly processes in histogenesis? Equilibrium configurations and the emergence of a hierarchy among populations of embryonic cells. J. Exp. Zool. *173*, 395–433. https://doi.org/10.1002/jez.1401730406.
83. Schwabe, T., Borycz, J.A., Meinertzhagen, I.A., and Clandinin, T.R. (2014). Differential adhesion determines the organization of synaptic fascicles in the Drosophila visual system. Curr. Biol. *24*, 1304–1313. https://doi.org/10.1016/j.cub.2014.04.047.
84. Hiesinger, P.R. (2021). Brain wiring with composite instructions. BioEssays *43*, e2000166. https://doi.org/10.1002/bies.202000166.
85. Rintelen, F., Stocker, H., Thomas, G., and Hafen, E. (2001). PDK1 regulates growth through Akt and S6K in Drosophila. Proc. Natl. Acad. Sci. USA *98*, 15020–15025. https://doi.org/10.1073/pnas.011318098.
86. Pecot, M.Y., Tadros, W., Nern, A., Bader, M., Chen, Y., and Zipursky, S.L. (2013). Multiple interactions control synaptic layer specificity in the Drosophila visual system. Neuron *77*, 299–310. https://doi.org/10.1016/j.neuron.2012.11.007.
87. Han, C., Jan, L.Y., and Jan, Y.N. (2011). Enhancer-driven membrane markers for analysis of nonautonomous mechanisms reveal neuron-glia interactions in Drosophila. Proc. Natl. Acad. Sci. USA *108*, 9673–9678. https://doi.org/10.1073/pnas.1106386108.
88. Özel, M.N., Langen, M., Hassan, B.A., and Hiesinger, P.R. (2015). Filopodial dynamics and growth cone stabilization in Drosophila visual circuit development. eLife *4*, e10721. https://doi.org/10.7554/eLife.10721.
89. Asano, S.M., Gao, R., Wassie, A.T., Tillberg, P.W., Chen, F., and Boyden, E.S. (2018). Expansion microscopy: protocols for imaging proteins and RNA in cells and tissues. Curr. Protoc. Cell Biol. *80*, e56. https://doi.org/10.1002/cpcb.56.
90. Chan, C.C., Scoggin, S., Wang, D., Cherry, S., Dembo, T., Greenberg, B., Jin, E.J., Kuey, C., Lopez, A., Mehta, S.Q., et al. (2011). Systematic discovery of Rab GTPases with synaptic functions in Drosophila. Curr. Biol. *21*, 1704–1715. https://doi.org/10.1016/j.cub.2011.08.058.
91. Pankiv, S., Clausen, T.H., Lamark, T., Brech, A., Bruun, J.A., Outzen, H., Øvervatn, A., Bjørkøy, G., and Johansen, T. (2007). p62/SQSTM1 binds directly to Atg8/LC3 to facilitate degradation of ubiquitinated protein aggregates by autophagy. J. Biol. Chem. *282*, 24131–24145. https://doi.org/10.1074/jbc.M702824200.
92. Matsubara, D., Horiuchi, S.Y., Shimono, K., Usui, T., and Uemura, T. (2011). The seven-pass transmembrane cadherin Flamingo controls dendritic self-avoidance via its binding to a LIM domain protein, Espinas, in Drosophila sensory neurons. Genes Dev. *25*, 1982–1996. https://doi.org/10.1101/gad.16531611.
93. Bolte, S., and Cordelières, F.P. (2006). A guided tour into subcellular colocalization analysis in light microscopy. J. Microsc. *224*, 213–232. https://doi.org/10.1111/j.1365-2818.2006.01706.x.

Please cite this article in press as: Kehribar et al., Selective adhesion preserves eye patterning as axonal retinotopy in the *Drosophila* brain, Current Biology (2026), https://doi.org/10.1016/j.cub.2026.01.007

CellPress
OPEN ACCESS

STAR★METHODS

KEY RESOURCES TABLE

REAGENT or RESOURCE	SOURCE	IDENTIFIER
Antibodies		
Mouse anti-chaoptin	Developmental Studies Hybridoma Bank (DSHB)	24B10; RRID: AB_528161
Mouse anti-Armadillo	DSHB	N2 7A1; RRID: AB_528089
Rat anti-Ecadherin	DSHB	DCAD2; RRID: AB_528120
Guinea pig anti-Sdk	Astigarraga et al.[59]	N/A
Rabbit anti-GFP	Thermo Fisher Scientific	RRID: AB_221569
Rabbit anti-Rap1	Thermo Fisher Scientific	Cat#: PA576317; RRID: AB_2720044
Chicken anti-GFP	Abcam	Cat#: AB13970; RRID: AB_2936447
Rabbit anti-dsRed	Takara Living Colors	Cat#: 632496; RRID: AB_10013483
Mouse anti-flamingo	DSHB	Flamingo 374; RRID: AB_2619583
Goat anti-mCherry	SICGEN	Cat#: AB0040-500; RRID: AB_2333093
Goat anti-rabbit Alexa Fluor 488	Jackson ImmunoResearch (West Grove, PA, USA)	Cat#: 111-545-003; RRID: AB_2338046
Donkey anti-rabbit Alexa Fluor 488 (for ExM)	Thermo Fisher	RRID: AB_2535792
Donkey anti-chicken Alexa Fluor 488	Jackson ImmunoResearch (West Grove, PA, USA)	Cat#: 703-545-155; RRID: AB_2340375
Goat anti-rat Cy3	Jackson ImmunoResearch (West Grove, PA, USA)	Cat#: 112-165-167; RRID: AB_2338251
Goat anti-mouse Cy5	Jackson ImmunoResearch (West Grove, PA, USA)	Cat#: 115-175-166; RRID: AB_2338714
Goat anti-mouse CF633 (for ExM)	Sigma-Aldrich	Cat#: SAB4600336; RRID: AB_3094754
Donkey anti-Goat Alexa Fluor 555 (for ExM)	Thermo Fisher	RRID: AB_2535853
Goat anti-guinea pig Cy3	Jackson ImmunoResearch (West Grove, PA, USA)	Cat#: 106-165-003; RRID: AB_2337423
Goat anti-rabbit Cy5	Jackson ImmunoResearch (West Grove, PA, USA)	Cat#: 111-175-144; RRID: AB_2338013
Goat anti-mouse Cy3	Jackson ImmunoResearch (West Grove, PA, USA)	Cat#: 115-165-166; RRID: AB_2338692
Chemicals, peptides, and recombinant proteins		
Vectashield	Vector Laboratories	Cat#: H-1000
PBS (also for ExM)	GIBCO	Cat#: 70011-36
Formaldehyde	Merch KGaA	Cat#: 1.03999.1000
Triton X-100 (also for ExM)	Sigma-Aldrich	Cat#: T8787
Agarose, low gelling temperature	Sigma-Aldrich	Cat#: A9045-10G
High vacuum grease	Dow Corning	Cat#: Z273554-1EA
4-Hydroxy-TEMPO (for ExM)	Sigma-Aldrich	Cat#: 176141
TEMED (for ExM)	Thermo Fisher Scientific	Cat#: 17919
Ammonium persulfate (APS) (for ExM)	Thermo Fisher Scientific	Cat#: 17874
Sodium acrylate (for ExM)	Thermo Fisher Scientific	Cat#: 408220
Acrylamide (for ExM)	Sigma-Aldrich	Cat#: A9909
N′N′methylenebisacrylamide (for ExM)	Sigma-Aldrich	Cat#: M7279
Sodium chloride (for ExM)	Roth	Cat#: 3957.1
EDTA (for ExM)	VWR Chemicals	Cat#: 20301.186
Tris-Cl (for ExM)	Roth	Cat#: 9090.2
Acryloyl-X-SE (for ExM)	Thermo Fisher Scientific	Cat#: A20770
DMSO (for ExM)	Thermo Fisher Scientific	Cat#: 326881000
Proteinase K (for ExM)	Thermo Fisher Scientific	Cat#: EO0491
Drosophila: GMR-FRT- w+-FRT-Gal4 (II)	Rintelen et al.[85]	N/A
Experimental models: Organisms/strains		
Drosophila: 9B08-Gal4	Pecot et al.[86]	N/A
Drosophila: mdelta0.5-Gal4	Gift from T. Clandinin	N/A
Drosophila: GMR-myrtdTomato (II and III)	Gift from S. Lawrence Zipursky	N/A

(*Continued on next page*)

Please cite this article in press as: Kehribar et al., Selective adhesion preserves eye patterning as axonal retinotopy in the *Drosophila* brain, Current Biology (2026), https://doi.org/10.1016/j.cub.2026.01.007

Continued

REAGENT or RESOURCE	SOURCE	IDENTIFIER
Drosophila: mdeltaGFP	Gift from T. Clandinin	N/A
Drosophila: hs-FLP (X)	Bloomington Drosophila Stock Center (BDSC)	RRID: BDSC_8862
Drosophila: UASCD4::tdGFP (II)	BDSC	RRID: BDSC_35839
Drosophila: UASCD4::tdGFP (III)	BDSC	RRID: BDSC_35836
Drosophila: UASCD4::tdTom (III)	BDSC	RRID: BDSC_35837
Drosophila: sdkMB05054 (X)	BDSC	RRID: BDSC_24603
Drosophila: sdkD15 (X)	Astigarraga et al.[59]	N/A
Drosophila: FRT19A (X)	Astigarraga et al.[59]	N/A
Drosophila: FRT19A, tubGal80 (X)	Astigarraga et al.[59]	N/A
Drosophila: Fmi-mCherry-pHluorin (II)	See STAR Methods: Endogenous Fmi-mCherry-pHluorin knock-in and Data S1.	N/A
Drosophila: lz-Gal4, UASmCD8GFP (X)	BDSC	RRID: BDSC_6314
Drosophila: GMR49A06-Gal4 (III)	BDSC	RRID: BDSC_50401
Drosophila: UAS-Fmi-RNAi (II)	Vienna Drosophila Resource Center (VDRC)	Cat#: KK-107993
Drosophila: FRT42D, fmiE59 (II)	BDSC	RRID: BDSC_41776
Drosophila: FRT42D (II)	Gift from S. Sigrist	N/A
Drosophila: fzP21, FRT2A (III)	Gift from G. Struhl	N/A
Drosophila: FRT2A, tubGal80 (III)	Gift from G. Struhl	N/A
Drosophila: dsUA071, FRT40 (II)	Gift from D. Strutt	N/A
Drosophila: FRT40, Gal80 (II)	Gift from D. Strutt	N/A
Drosophila: UAS-myrtdTom (II)	BDSC	RRID: BDSC_32222
Drosophila: tub-Gal4 (III)	Gift from C. Dahlmann	N/A
Drosophila: yw (X)	Gift from J. Treisman	N/A
Drosophila: UAS-Sdk-RNAi (II)	VDRC	9437
Drosophila: UAS-mCD8GFP (X)	Gift from C. Dahmann	N/A
Drosophila: GMR-Gal4 (III)	Han et al.[87]	N/A
Drosophila: UAS-deGradFP (III)	BDSC	RRID: BDSC_38421
Software and algorithms		
Amira	FEI-Thermo Fisher Scientific	RRID: SCR_014305
ImageJ	National Institutes of Health (NIH)	RRID: SCR_002285
GraphPad Prism 10	GraphPad Software	RRID: SCR_002798
Photoshop CS6	Adobe Systems Incorporated	RRID: SCR_014199
Unity game engine	Unity Technologies	N/A
Matplotlib 3.10.1	Matplotlib	RRID: SCR_008624
Python 3.12.3 with NumPy 2.2.4	Python	RRID: SCR_008394
Deposited data		
Code for computational simulations	Zenodo	https://doi.org/10.5281/zenodo.15561406.

EXPERIMENTAL MODEL AND STUDY PARTICIPANT DETAILS

Fly husbandry and genetics

All flies were kept on standard food at 25°C. To study specific developmental stages, white pupae at P0 (0h after puparium formation) were collected from their vials and aged at 25°C until the desired stage. Male and female pupae were collected equally, unless otherwise stated (see *sdk*- experiments in Table S1). All source details of all fly lines are provided in the key resources table, all genotypes are listed in Table S1 in the supplemental information.

METHOD DETAILS

Histology and fixed imaging

All brains were dissected in phosphate-buffered saline (PBS, pH=7.4) and immediately fixed in 4% paraformaldehyde (PFA) in PBS for 30 minutes at room temperature. Next, they were washed with PBST (0.4% Triton-X in PBS) three times short

Please cite this article in press as: Kehribar et al., Selective adhesion preserves eye patterning as axonal retinotopy in the *Drosophila* brain, Current Biology (2026), https://doi.org/10.1016/j.cub.2026.01.007

and kept on a shaker at room temperature for at least 6 hours. Specimens were incubated with primary antibody for 24-48 hours and washed thereafter with PBST again, following the same procedure as before. Subsequently, they were incubated with secondary antibodies for another 24-48 hours and again washed with PBST following the same procedure. Next, brains were kept on a shaker at room temperature for 2-4 hours and mounted in Vectashield (Vector Laboratories, CA). All antibodies are listed in Table S2 in the supplemental information.

All samples were scanned with a Leica TCS SP8-X white light laser confocal microscope that is equipped with a 63X glycerol objective (NA=1.3). All expanded samples were imaged with the same confocal microscope with a 40X water objective (NA=1.3).

Antibody screening

We screened the whole catalog of *Drosophila* antibodies from Developmental Studies Hybridoma Bank (DSHB) as well as some other antibodies for proteins that were previously known to be expressed in the lamina plexus (such as Sdk). This consisted of over 280 antibodies, including more than 20 known adhesion molecules.

Ex-vivo brain cultures

Brains were dissected in chilled Schneider's *Drosophila* Medium and kept in oxygenized chilled culture medium (1:10 fetal bovine serum (FBS), 10 mg/ml human insulin recombinant zinc (Stock: 4 mg/ml), 1:100 Penicillin/streptomycin (Stock: 10000 IU/ml penicillin, 10 mg/ml streptomycin), 1 mg/ml 20-Hydroxyecdysone (Stock: 1 mg/ml in ethanol) in Schneider's Drosophila Medium) until mounting in culture chambers (60x15 mm petri dish lids with a layer of Sylgard 184 (Dow Corning) at the center (2 cm in diameter). For mounting, brains were placed at the center of the Sylgard layer in a 30ul drop of 0.4% dialyzed low melting agarose in oxygenized culture medium (34°C), 200 mm thick X-ray films cut in 1x1 mm pieces were used as spacers between brain and coverslip (circular, 4 cm diameter), which was glued to the petri dish at 3 points using rubber cement. After 15 min, the space between coverslip and the petri dish was filled with oxygenized culture medium and the chamber completely sealed with rubber cement and let rest for 1h.

Live imaging was performed at 25°C using a Leica SP8 MP microscope with a 40X IRAPO water objective (NA = 1.1), a Chameleon Ti:Sapphire laser (Coherent) and a resonant scanner at 30 min time intervals. Excitation wavelength were 870 nm and 1090 nm for GFP and Tomato, respectively. For more detailed information also see Özel et al.[88]

2-photon intravital live imaging

All intravital imaging samples were prepared as described before.[17] Briefly, the pupal case around the head of a pupa, which was staged until P14-17 was removed. Then the pupa was stabilized on its right side by a multi layered cast that was formed by Whatman (Fisher Scientific) papers. For comparability between samples, the left eye was scanned always. High vacuum grease (Dow Corning Corporation) was applied around the cast as a spacer for the cover slip. 1.5 μl PBS was put on a cover slip (VWR micro cover glass, 22x22 mm, No.1.5) and this cover slip was placed on the left eye such that PBS formed a layer between the eye and the cover slip. Live imaging was performed by utilizing a Leica SP8 multi-photon microscope equipped with a 40X IRAPO water objective (NA=1.1) and a Chameleon Ti:Sapphire laser (Coherent), whose power was controlled by an electro-optic modulator (EOM) for minimal bleaching. For two-color imaging of GFP and Tomato, excitation wavelength was set to 870 nm and 1090 nm for GFP and Tomato, respectively. The microscope stage was in a closed chamber and the temperature inside the chamber was controlled by an environment controller and always set to 25°C during imaging. Time resolutions of the scans were set between 10-30 min depending on the total imaging time period. Flies were imaged until P35-40 and then kept until they hatched into functional adults.

Expansion microscopy

For expansion of whole fly brains, we followed the "*Basic Protocol 2: proExM for Intact Tissues*" from Asano et al.[89] with minor changes in handling and mounting of the samples implemented by us. Brains were dissected, fixed, and stained before expansion. For expansion, the reagents denoted with "for ExM" in the key resources table were used. Samples were mounted on Sylgard slides, where all excess water was removed using tissue paper (Kim Wipes, Kimtech). If necessary, 2% agarose gel was heated up and carefully pipetted around the sample to stop it from moving around.

Endogenous Fmi-mCherry-pHluorin knock-in

Endogenous fmi was tagged using the recombineering protocol in Chan et al.[90] We first subcloned the entire *fmi* locus, which was sourced from a bacterial artificial chromosome (CH321-66D09),[34] into a P[acman]-KO vector. We then replaced Gal4 sequence in the original Gal4-3×P3-RFP-Kanamycin cassette[90] with an mCherry-pHluorin segment that was based on the mCherry-EGFP construct from Pankiv et al.[91] A Gly-Ser linker (GGGSGGGSGGGS)[92] followed by the mCherry-pHluorin-3×P3-RFP-Kanamycin cassette was knocked-in in place of the stop codon of the fmi-RA-isoform in the P[acman]-KO vector. After inserting the tagged *fmi* on the 3rd chromosome, we mobilized the tagged allele and retargeted it into the endogenous *fmi* locus on 2nd chromosome following the recombineering protocol.[90] Finally, the 3×P3-RFP-Kanamycin selection marker was excised by Cre/loxP recombination and confirmed by PCR.

The final sequence at the insertion site can be found in Data S1.

Please cite this article in press as: Kehribar et al., Selective adhesion preserves eye patterning as axonal retinotopy in the *Drosophila* brain, Current Biology (2026), https://doi.org/10.1016/j.cub.2026.01.007

Computational modeling – atom model

We performed agent-based simulations (Euler-Maruyama) of particles interacting via three forces: (i) sidekick and (ii) flamingo were formalized by Ricker wavelets with sigma=36 and amplitudes of 1000 and 100, respectively. Additionally, (iii) density repulsion was implemented via an inverted-parabola kernel with width 0.4*sigma and amplitude 100. The receptor heels were spawned in sequence: R2/R5 first, R3/4 two hours later, R1/R6 another two hours later. Different rows were separated by two hours, i.e. R3/R4 in the first row and R2/R5 in the second row appeared at the same time. The temporal succession of flamingo forces was as sketched in Figure 7B. For the first two hours, R2/R5 are held in place by a flamingo force, anchoring them to R8 until R3/R4 arrive.

We used two-dimensional simulations of atomic forces, where the axonal arrival points (heels) were treated as 'atoms' which interact via circular potentials. In addition to flamingo and sidekick, we included 'density kernels' to avoid overlap between heels that do not directly interact via flamingo or sidekick. Together, these three forces were sufficient to (i) create and maintain a stable pattern, (ii) reproduce the biologically observed bundle rotation for central rows of the pattern, and (iii) gradually shift the bundle shape from circular to 'horseshoe' shaped. However, attempts to make the pattern grow led to strong distortion of the bundle (horseshoe) shapes. This is likely due to the absence of extended membrane-to-membrane contacts between heels, which would occur in biology but are not part of the atomic simulations. Circular potentials provided more freedom for the movement of heels than longer stretches of membrane that were tightly connected via flamingo or sidekick. To include these extended membrane-to-membrane contacts in the model, we turned to the Unity game engine o simulate soft bodies with adhesive, flexible surfaces.

Computational modeling – soft body model

This simulation was developed in Unity (version 2022.3.6f1, U. Technologies, Unity Real-Time Development Platform | 3D, 2D VR & AR Engine. [Online.] Available: https://unity.com/). The environmental physics were configured with zero gravity and default settings. A central spawner object controls initial conditions: number of rows, objects per row, spatial/temporal parameters. The simulation follows the known differentiation order of R cells: first, R8 cells spawn in a zigzag, initiating the growth of R2/R5, then R3/R4, followed by R1/R6. Each new row's R8's appearance is dependent the previous one. In equator simulation, the same procedure applies but the spawning pattern is mirrored in the center.

Soft body physics were added to allow realistic deformation and interaction. This feature was modeled after a tutorial (PyroPhysics, How to Make Softbody Physics in Unity!, Feb. 2021. [Online.] Available: https://www.youtube.com/watch?v=3avaX00MhYc&t=1s&ab_channel= PyroPhysics). Circle sprites were rigged with bones (RigidBody2D (U. Technologies, Unity- Manual: Rigid Body 2D, en. [Online]. Available: https: //docs.unity3d.com/Manual/rigidbody2D.html) + CircleCollider2D (U. Technologies, Unity- Manual: Circle Collider 2D, en. [Online]. Available: https://docs.unity3d.com/Manual/class-CircleCollider2D.html)) and connected via SpringJoint2D (U. Technologies, Unity- Manual: Spring Joint 2D, en. [Online] Available: https://docs.unity3d.com/Manual/class-SpringJoint2D.html) to simulate elasticity. Growth functions allow temporal expansion, signaling "arrival" in the lamina. R8 remains smallest (0.2 units), followed by R3/R4 (0.6 units), and others at full size (1 unit). The model occasionally exhibits overlapping growth ("clipping") which is considered biologically plausible background adhesion and thus retained.

An additional model was created to simulate a case where no non-R cell space is allowed, thereby minimizes empty space occupied by L cells; this was achieved with a physical border around the spawning R cell terminals and a force which creates additional adhesion.

Adhesion between cells was modeled using SpringJoint2D connections. Early Flamingo (Fmi) adhesion connects R2, R5, and R8 upon collision, breaking when R1/R6 intercalate. Late Flamingo activates after 20% R1/R6 growth and adds R2-R6 and R1-R5 connections. Sidekick (Sdk) models intra-bundle adhesion (excluding R1-R6 connection) and has a higher break force, remaining constant throughout development. Mutations were simulated by setting the respective adhesive forces to 0. Additionally, for the mutant simulations with simulated axonal defects in the optic stalk: In case of *fmi*- simulation, bundles are rotated upon arrival and both early and late Fmi are turned off. In *sdk*- simulation, Sdk adhesion is turned off in all heels, for R1s, R3s, R4s and R6s positions random noise is added upon arrival and for R3 and R4 some are swapped into neighboring bundles upon their arrival. Double mutant simulation contains both properties.

Data from 100 simulations (with/without mutations) were analyzed in R (R Core Team (2024). R: A Language and Environment for Statistical Computing. R Foundation for Statistical Computing, Vienna, Austria. <https://www.R-project.org/>). Average heel positions and standard deviations were calculated to assess pattern robustness.

Animation of retinotopic map formation

The graphical abstract animation video was created using Blender 4.5 (Blender Foundation, Amsterdam, Netherlands). The modeling and animation were based on the geometry nodes system. The structures and processes shown in the video are based on the data and illustrations described within this study and in Chang et al.[42] and serve to visualize the mechanisms.

QUANTIFICATION AND STATISTICAL ANALYSIS

Equator analysis

To compare equator patterns of the eye and the underlying lamina plexus, we marked the respective patterns as follows: single cell clones were generated using an FRT-flanked stop cassette in a GMR-FRT-w+-FRT-Gal4 construct that was excised using a heat

Please cite this article in press as: Kehribar et al., Selective adhesion preserves eye patterning as axonal retinotopy in the *Drosophila* brain, Current Biology (2026), https://doi.org/10.1016/j.cub.2026.01.007

shock mediated expression of flipase. Larvae were heat shocked for 6-8 minutes at 37°C, 2-4 days after egg laying. This resulted in single photoreceptors labeled with Tomato that could be traced from their cell body position in the eye to their axon terminals in the lamina plexus. To determine the turn of the equator to either left or right in each row, all R4 cells were labeled using mdelta0.5-eGFP,[28] and their polarization either to (LP) or away (eye) from the equator was used. In the lamina plexus, R4 growth cones at the equator overlap significantly, so an additional tool was used to identify each turn: Arm staining labels contact points of R cell heels (similar to Sdk and Ecad), thus creating a horseshoe shape that points towards the equator on both sides.

Quantification of correlation between Fmi and R cell subtypes

To quantify the correlation between Fmi signal and different R cell subtypes, we used the Image J Plugin „JACoP"[93] (https://imagej.net/ij/plugins/track/jacop2.html, Image J) to calculate the Pearson's coefficient. The coefficient estimates a "goodness" of the approximation of the rate of association between two fluochromes – in this case, the GFP channel (R cell subtype) and the red channel (Fmi staining). The value ranges from 1 to -1, with 1 standing for complete positive correlation, 0 for no correlation, and -1 for complete negative correlation. For our quantification, we used three images per subtype and calculated the mean Pearson's coefficient +- SEM, shown in Figure 2I.

fmi- axon arrival analysis

To quantify the arrival defect in *fmi*- axons, we generated 2D images of the same clonal patch for all time points of our live imaging data set. We then measured the distance of the stalled axons to the lamina plexus for each time point and plotted the distance against the developmental time (pupal stage).

Bundle distance analysis

In *fmi*-MARCM experiments, bundle distance was measured by firstly marking the center of each bundle using Sdk or Ecad staining: Both label contact points of R cell heels thus creating a horseshoe shape, which was marked as the bundle center. Subsequently, bundles were linked to their neighbors in diagonal rows (see Figure 4A′) with a line that was then measured to determine bundle distance.

Intrabundle R4 position analysis in the lamina plexus

To determine R4 positions in bundles, R4s were labeled using mdelta0.5-eGFP and Ecad staining was used to mark growth cone contact points inside each bundle. Then, connecting the contact points between R6 and R5 and between R1 and R2, a bundle center was determined, which was then connected to the R4 arrival point in the bundle. The angle between the center and the R4 was then used as intrabundle R4 position and compared between experimental and control regions. As Ecad is downregulated in *sdk*- bundles, we instead used Arm staining which labels L cells. We used this to identify the bundle center and the angle to the labeled R4 was measured from there.

In ommatidia, R7 cell bodies were identified based on their position in the rhabdomere pattern and marked. From there, R4 cell bodies labeled with mdelta0.5-eGFP were connected and the angle was measured.

Braiding analysis

To identify a single axon's position inside of an axon bundle, we used 24B10 staining to label the membranes of the R cell axons. Additionally, we labeled R4s with mdelta0.5-Gal4 expressing UAS-myrtdTom. We then went through a scanned z stack that spanned about 15-20 microns between the retina and lamina plexus, frame by frame, with a z step size of 0.25μm.

Identifying inter-bundle pattern in *sdk* mutants

Because the R2/5/8 driver line GMR49A06-Gal4 occasionally shows expression in R4 cells, we separately labeled R4s in the same samples using mdelta-eGFP - a fusion construct that does not interfere with the Gal4-UAS system. To label R2/5/4 cells, we used GMR49A06-Gal4 driving UAS-CD4tdTomato. To distinguish R2/5 from R4 cells, we created 2D images of the lamina plexus and binarized both the GFP and Tomato channels. We then subtracted the GFP mask (R4s) from the Tomato mask (R2/5/4) and multiplied the resulting mask with the original Tomato channel. This produced a new Tomato channel that excluded any cells co-expressing both markers - i.e., R4s. The resulting channel specifically marks R2/5 cells, allowing us to analyze their positions and identify inter-bundle patterns.

Fmi-mCherry-pHluorin levels in the lamina plexus

To compare levels of „active" Fmi (green/yellow) to levels of Fmi in degradative compartments (red only) through development, first, the live dataset was manually segmented into two separate labels for each time point: Lamina cortex and lamina plexus. Then, a threshold was set to ensure that only the actual signal was captured by the analysis without measuring the background noise of the data. The remaining signal was processed using the Material Statistics tool of the Amira software, which measured the following parameters of the labels: Count, volume, minimum value, maximum value, center-X, -Y, -Z, mean, deviation, variance, and cumulative sum. These values were measured for each category: green signal, total red signal (yellow), and red only signal, for lamina cortex and lamina plexus, respectively. For the graph shown in Figure S2H, the count of each channel was plotted against the volume of the whole label (y axis) and shown per time point (x axis).

Please cite this article in press as: Kehribar et al., Selective adhesion preserves eye patterning as axonal retinotopy in the *Drosophila* brain, Current Biology (2026), https://doi.org/10.1016/j.cub.2026.01.007

Quantification and data analysis

All fixed and live imaging raw data were analyzed with Amira 5.6 (Thermo Fisher Scientific). Segmentation of lamina plexus were done manually using the segmentation tool of Amira. For videos made from live imaging data sets, individual frames were first created with Amira 5.6 and then aligned for misalignments between time points in Photoshop CS6 (Adobe). All distance and angle measurements were done using Image J (NIH).

Quantification of L cell shapes in computational model and biological data

To compare the L cell shapes between model and data, we first extract all occurrences of L cell shapes from the L cell channel of the data using OpenCV's template matching function (threshold=0.55) with the shape from Figure 7G′ as template. Similarly, we create a set of model shapes with the shape from Figure 7F′ as template. In both sets (for data and model), images are processed to only contain the central L cell shape and a threshold is applied (135 in [0... 255] grey-scale images) to obtain binary images. Shapes are required to contain a minimum of 200 pixels. The final sets of L cell shapes contain N=169 (data) and M=46 (model) shapes, resulting in NxM=7774 comparisons. We calculate the Intersection over Union (IoU), Hausdorff distance, and log distance of the Hu moments for all pairs. For the former two, we align the center of masses of the two compared shapes and scale the shapes to share the same bounding box. The Hu moments are translation- and scaling-invariant by definition. To obtain null distributions for the three quantities, we create a set of random shapes: polygons with 4 to 10 corners and Fourier shapes 3 to 7 random coefficients. The number of corners and coefficients is randomly drawn (from a uniform distribution) for each random shape. We create 200 random polygons and 200 random Fourier shapes. The 400 random shapes are then compared to the L cell shapes from the data, resulting in a null distribution for the three similarity measures. We report the medians of all distributions and use the Mann-Whitney rank test for statistical comparison.

Statistical analysis

All graphs corresponding to analyzed data were created with Prism 10 (GraphPad).

To test statistical difference in variances, t-tests and F-tests were used. To compare multiple groups, one-way Anova tests were used. This includes Fmi correlation with subtypes, bundle distance analyses, R4 intra-bundle and R4 intra-ommatidial position analyses. First, data was tested for normality using normality and lognormality tests. Depending on normality, either an unpaired t test (normal distribution) or Mann-Whitney and Kolmogorov-Smirnov tests (not normal) were used. The number of the optic lobes that were quantified or examined are given in the figure legends. Error bars and p values are described in the respective figure legends.